Light-induced shear phonon splitting and instability in bilayer graphene

Habib Rostami [*]

Department of Physics, University of Bath, Claverton Down, Bath BA2 7AY, United Kingdom
and Nordita, KTH Royal Institute of Technology and Stockholm University, Hannes Alfvéns väg 12, 10691 Stockholm, Sweden

Coherent engineering of landscape potential in crystalline materials is a rapidly evolving research field. Ultrafast optical pulses can manipulate low-frequency shear phonons in van der Waals layered materials through the dynamical dressing of electronic structure and photoexcited carrier density. In this work, we provide a diagrammatic formalism for nonlinear Raman force and implement it to shear phonon dynamics in bilayer graphene. We predict a controllable splitting of double degenerate shear phonon modes due to light-induced phonon mixing and renormalization according to a coherent nonlinear Raman force mechanism. Intriguingly, we obtain a light-induced shear phonon softening that facilitates structural instability at a critical field amplitude for which the shear phonon frequency vanishes. The phonon splitting and instability strongly depend on the laser intensity, frequency, chemical potential, and temperature of photoexcited electrons. This study motivates future experimental investigation of the optical fine tuning and regulation of shear phonons and layer stacking order in layered van der Waals materials.

I. INTRODUCTION

Exotic emergent phenomena in quantum systems can be generated via photoexcitation by ultrafast optical drives [1–5]. Depending on the intensity of the pump laser, we can excite and disentangle collective modes, switch the macroscopic phase of the system, dynamically engineer critical phenomena, and render robust nonlinear couplings among the different degrees of freedom in the quantum materials [6–8]. Optical switching and photoinduced transitions correspond to the dynamical modification of the free energy landscape that is not accessible in thermal equilibrium. Photoinduced nonthermal and coherent control of correlated and topological quantum materials [9] is being under investigation in multiple ways, such as Floquet-Bloch dressed single-particle states [10] and optical dressing of many-body interaction couplings [11,12]. Manipulating and fine tuning the structural phase of quantum materials by ultrashort laser pulses opens a pathway to regulate quantum devices. For instance, substantial lattice deformations are reported induced by intense midinfrared optical pulse irradiation, e.g., dynamically generated ferroelectricity and shear strain [13,14]. Large photoinduced deformations are due to resonance with a vibration mode, strong Raman force, and nonlinear phonon couplings [8,13–17].

---
[*]hr745@bath.ac.uk

Shear phonons in bilayer [see Fig. 1(a)] and multilayer of two-dimensional (2D) materials, such as the family of graphene, transition-metal dichalcogenides (TMDs), and hexagonal boron nitride (hBN), correspond to the lateral sliding of atomic layers on each other [18–26]. Shear phonon
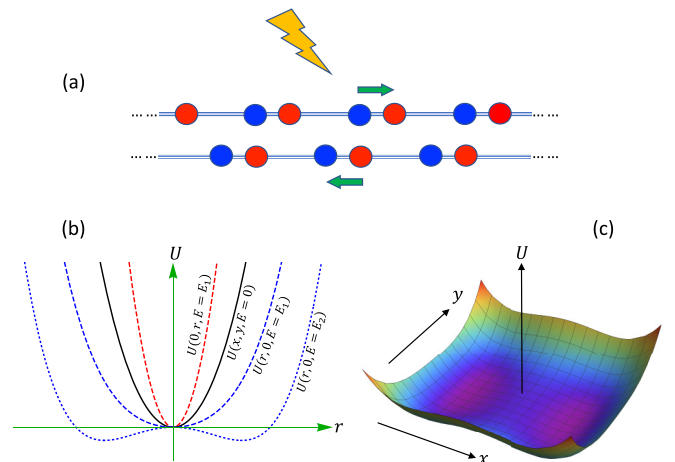

FIG. 1. Schematic picture of the setup and the shear potential. (a) Light-indued shear phonon displacement in a bilayer system induced. (b) Modification of the landscape shear potential due to the incident light, where initially degenerate shear modes along the x and y directions in the absence of the light field ($E = 0$) can be split at an electric field amplitude of $E = E_1$, or a more dramatic change can occur in one of the modes, leading to instability at a stronger electric field amplitude of $E_2 > E_1$. (c) A saddlelike shear potential at the origin exhibits both stable and unstable modes polarized along the y and x directions, while a pair of stable modes emerge along the x direction.

excitation can coherently alter the staking order of layers [27,28], and the electronic topology [29]. Light-induced displacive dynamics [30–41] of coherent shear phonons in van der Waals (vdW) layered materials such as multilayer graphene, WTe$_2$, and MoTe$_2$ [27–29,42–45] is a promising nondestructive mechanism for controlling 2D materials properties. The shear mode in bilayer graphene is a double degenerate Raman-active optical mode and it has a low frequency $\hbar\Omega_0 \approx 3.9$ meV due to the weak vdW interlayer force [18]. The energy and the intensity of the Raman peak for the shear mode (the C peak) strongly depend on the number of layers and interlayer coupling. Accordingly, the spectroscopy of interlayer Raman modes is an effective method for determining layer numbers and stacking configurations, and it provides a unique opportunity to explore interlayer couplings. Driving coherent shear phonon in MoTe$_2$ causes a first-order phase transition from an inversion symmetric 1T′ structure to the noncentrosymmetric 1T$_d$ phase [27,44]. Time- and angle-resolved photoemission spectroscopy (tr-ARPES) of the Weyl semimetal T$_d$-WTe$_2$, indicates coherent shear phonon-mediated control of the electronic structure [45]. An optical switching from an ABA to ABC stacking is experimentally obtained by laser irradiation on trilayer graphene [42] that might be because of the coherent shear phonon excitation.

This paper studies the dynamical engineering of lattice potential for the shear dynamics in vdW layered materials caused by a linear polarized light field $\mathbf{E}(t)$. The impact of second- and third-order Raman susceptibilities gives rise to light-induced corrections to the lattice potential:

$$U = \frac{1}{2}\sum_{\alpha\beta}\left[\Omega_0^2\delta_{\alpha\beta} - \mathcal{G}_{\alpha\beta}(\mathbf{E})\right]Q_\alpha Q_\beta - \sum_\alpha \mathcal{F}_\alpha^{(2)}(\mathbf{E})Q_\alpha, \quad (1)$$

where $\mathbf{Q} = (Q_x, Q_y)$ is the shear phonon displacement with Ω_0 being the unperturbed phonon frequency. Displacive Raman shear force described as a second-order effect $F^{(2)} \propto EE^*$ in bilayer graphene has been previously investigated [46]. Here, we define the third-order Raman shear force as $F^{(3)} = \overset{\leftrightarrow}{G} \cdot \mathbf{Q} \propto QEE^*$, which can renormalize shear phonons and lead to a mode splitting. In particular, it can cause the instability of atomic layers to slide and form stable or metastable phases with different layer-stacking orders due to the softening of shear phonon frequency under the influence of the light field. The $\mathcal{G}_{\alpha\beta}$ coupling can be interpreted as a light-induced self-energy correction $\Sigma_{\alpha\beta}(\mathbf{E}) = -\mathcal{G}_{\alpha\beta}(\mathbf{E})/2\Omega_0$ to the phonon's dynamical matrix. As the central result, here, we develop a diagrammatic formalism to model the impact of third-order Raman force (or light-induced phonon self-energy) on the displacive dynamics of shear phonons in layered materials. We obtain a dynamical renormalization of the shear phonons by incident light intensity leading to the splitting of the double degenerate shear phonons. We predict a lattice instability where the shear phonon frequency vanishes at a critical field amplitude, see schematic illustration of the optically modified shear potential in Figs. 1(b), and 1(c). We show that the field-induced phonon splitting and instability are highly tunable by the incident laser intensity, frequency at given electronic doping, and temperature. Our theoretical model based on the nonequilibrium

Green's function can be systematically employed in *ab initio* computations to study the optical engineering of shear phonon in layered materials.

The rest of the paper is structured in four sections. In Sec. II, we provide details of the diagrammatic method for the third-order Raman force and develop a perturbative theory for optically dressed phonon's dynamical matrix. In Sec. III, we summarize the mixed couplings of electrons, phonons, and photons in addition to light-matter and electron-phonon couplings in bilayer graphene. In Sec. IV, we discuss numerical results for the light-induced phonon renormalization and, thus, its effect on the optical modulation of the shear phonon spectral function, shear mode splitting, and the light-induced shear instability. Finally, we summarize our theoretical finding, discuss it in connection with experiments, and highlight the implication of light-induced phonon renormalization in other heterostructures of 2D materials.

II. METHOD

Stimulated Raman effect is an efficient mechanism to excite Raman-active vibrational modes [47]. The dipole moment of Raman-active phonon is linearly proportional to the light field $\mu_b = \alpha_{bc}E_c$ where the polarizability tensor α_{bc} depends on the phonon displacement vector $\mathbf{Q}$. The electromagnetic potential energy thus follows $U = -\mu_b E_b = -\alpha_{bc}E_b E_c$. The corresponding Raman force driving atoms to oscillate follows a second-order nonlinear process [47]

$$\mathcal{F}_a^{(2)} = -\left[\frac{\partial U}{\partial Q_a}\right]_{Q\to 0} = \sum_{bc}\left[\frac{\partial\alpha_{bc}}{\partial Q_a}\right]_{Q\to 0}E_b E_c. \quad (2)$$

Therefore the lowest-order Raman force is finite as long as the Raman susceptibility is nonvanishing, i.e., $\sigma_{abc}^{(2)} = \partial\alpha_{bc}/\partial Q_a \neq 0$. For large displacement, the higher-order Raman force should also be considered, which can dramatically impact phonon renormalization and lattice dynamics. The leading higher-order Raman force depends linearly on the phonon displacement and quadratically on the light field. Therefore, it is described by a third-order nonlinear mechanism

$$\mathcal{F}_a^{(3)} = \sum_{bcd}\left[\frac{\partial^2\alpha_{cd}}{\partial Q_a\partial Q_b}\right]_{Q\to 0}Q_b E_c E_d. \quad (3)$$

Formally, we have $\mathcal{F}_a^{(3)} = \mathcal{G}_{ab}Q_b$ in which $\mathcal{G}_{ab}$ generates a phonon self-energy in terms of a third-order Raman susceptibility $\sigma_{abcd}^{(3)} = \partial^2\alpha_{cd}/\partial Q_a\partial Q_b$ and the incident light intensity. An anisotropic $\mathcal{G}_{ab}$ breaks the degeneracy of Cartesian shear modes and renormalizes the phonon's frequency and linewidth.

To model coherent shear phonons in bilayer systems, we first provide a general theory for the Raman force and phonon self-energy using the Green's function method and diagrammatic framework. We decompose the total Hamiltonian of the system in different parts $\mathcal{H} = \mathcal{H}_e + \mathcal{H}_p + \mathcal{H}_{e-p} + \mathcal{H}_{lm}$ which consists of electronic kinetic Hamiltonian $\mathcal{H}_e$, harmonic phonon Hamiltonian $\mathcal{H}_p$, electron-phonon interaction $\mathcal{H}_{ep}$, and finally the light-matter interaction $\mathcal{H}_{lm}$. The electronic kinetic Hamiltonian reads $\hat{\mathcal{H}}_e = \sum_{\mathbf{p}}\hat{\psi}_{\mathbf{p}}^\dagger\hat{\mathcal{H}}(\mathbf{p})\hat{\psi}_{\mathbf{p}}$ where $\hat{\psi}_{\mathbf{p}}$ is the fermion annihilation spinor field at momentum $\mathbf{p}$. The harmonic shear phonon Hamiltonian with zero momen-

tum $\mathbf{q} = \mathbf{0}$ can be written in terms of ladder operators $\hat{\mathcal{H}}_p = \sum_\lambda \hbar\Omega_0 \hat{b}_\lambda^\dagger \hat{b}_\lambda$ where $\hat{b}_\lambda$ is the phonon annihilation operator. We only consider the zone center phonon modes with a vanishing wave vector $\mathbf{q} = \mathbf{0}$, and thus the phonon displacement vector is defined as

$$\hat{Q}_\lambda = \sqrt{\frac{\hbar}{\rho S \Omega_0}} (\hat{b}_\lambda + \hat{b}_\lambda^\dagger) \tag{4}$$

in which $\lambda = x, y$ indicates two Cartesian mode components. Note that S stands for the area of 2D material, and ρ is the mass density. Including both one-phonon and two-phonon couplings to electrons, the electron-phonon interaction Hamiltonian follows

$$\hat{\mathcal{H}}_{e-p} = \sum_{\mathbf{p}} \sum_a \hat{\psi}_{\mathbf{p}}^\dagger \hat{\mathcal{M}}_a^{(1)}(\mathbf{p}) \hat{\psi}_{\mathbf{p}} \hat{Q}_a$$
$$+ \sum_{\mathbf{p}} \sum_{ab} \hat{\psi}_{\mathbf{p}}^\dagger \hat{\mathcal{M}}_{ab}^{(2)}(\mathbf{p}) \hat{\psi}_{\mathbf{p}} \hat{Q}_a \hat{Q}_b. \tag{5}$$

Note that $\hat{\mathcal{M}}_a^{(1)}$ and $\hat{\mathcal{M}}_{ab}^{(2)}$ stand for the one- and two-phonon-electron coupling's matrix elements, respectively. Utilizing this effective lattice potential and the Heisenberg equation of motion, we obtain the equation of motion for coherent phonon displacement amplitude Q_a:

$$\frac{\partial^2 Q_a(t)}{\partial t^2} + \Gamma_p \frac{\partial Q_a(t)}{\partial t} + \Omega_0^2 Q_a(t)$$
$$= \frac{\mathcal{F}_a^{(2)}(t)}{\rho} + \frac{1}{\rho} \sum_b \mathcal{G}_{ab}^{\text{ins.}}(t) Q_b(t)$$
$$+ \frac{1}{\rho} \sum_b \int dt' \mathcal{G}_{ab}^{ret.}(t, t') Q_b(t'), \tag{6}$$

where Ω_0 is the shear phonons frequency, Γ_p stands for the phenomenological damping frequency of phonons. The leading-order Raman force is given as the expectation value of the one-phonon coupling to electrons:

$$\mathcal{F}_a^{(2)}(t) = -\frac{1}{S} \sum_{\mathbf{p}} \langle \hat{\psi}_{\mathbf{p}}^\dagger \hat{\mathcal{M}}_a^{(1)}(\mathbf{p}) \hat{\psi}_{\mathbf{p}} \rangle \big|_{\mathbf{Q} \to \mathbf{0}}. \tag{7}$$

The nonlinear force reveals two different dynamical forms of the light-induced phonon self-energy term $\mathcal{G}_{ab}$ that we label as instantaneous $\mathcal{G}_{ab}^{\text{ins.}}(t)$ and retarded $\mathcal{G}_{ab}^{ret.}(t, t')$ couplings. The instantaneous coupling is obtained as the expectation value of the two-phonon coupling matrix element

$$\mathcal{G}_{ab}^{\text{ins.}}(t) = -\frac{1}{S} \left[\sum_{\mathbf{p}} \langle \hat{\psi}_{\mathbf{p}}^\dagger \hat{\mathcal{M}}_{ab}^{(2)}(\mathbf{p}) \hat{\psi}_{\mathbf{p}} \rangle \right]_{\mathbf{Q} \to \mathbf{0}}. \tag{8}$$

While the retarded coupling is given by the variational derivative of the Raman force versus the phonon displacement field:

$$\mathcal{G}_{ab}^{ret.}(t, t') = -\frac{1}{S} \left[\frac{\delta}{\delta Q_b(t')} \sum_{\mathbf{p}} \langle \hat{\psi}_{\mathbf{p}}^\dagger \hat{\mathcal{M}}_a^{(1)}(\mathbf{p}) \hat{\psi}_{\mathbf{p}} \rangle \right]_{\mathbf{Q} \to \mathbf{0}}. \tag{9}$$

Note that $\langle \dots \rangle$ indicates quantum statistical averaging. In centrosymmetric systems, Raman-active phonons are infrared-inactive; therefore, they couple to light indirectly. The direct

light-matter interaction is only through the coupling to electrons. The coupling of incident light field to electrons can be modeled by Peierls substitution $\mathbf{p} \to \mathbf{p} + e\mathbf{A}(t)$ in the kinetic and the electron-phonon interaction Hamiltonian terms. Considering the homogeneous vector potential $\mathbf{A}(t)$, the electric field reads $\mathbf{E}(t) = -\partial_t \mathbf{A}(t)$ and thus $\mathbf{E}(\omega) = i\omega \mathbf{A}(\omega)$. Formally, the light-matter interaction Hamiltonian consists of two parts: Photon-electron term and photon-electron-phonon term $\hat{\mathcal{H}}_{lm} = \hat{\mathcal{H}}_{ph-e} + \hat{\mathcal{H}}_{ph-e-p}$. The photon-electron term follows

$$\mathcal{H}_{ph-e} = -\sum_{\mathbf{p}} \hat{\psi}_{\mathbf{p}}^\dagger \left\{ \sum_a \hat{j}_a(\mathbf{p}) A_a(t) \right.$$
$$\left. + \frac{1}{2} \sum_{ab} \hat{\gamma}_{ab}(\mathbf{p}) A_a(t) A_b(t) + \dots \right\} \hat{\psi}_{\mathbf{p}}, \tag{10}$$

where $\hat{j}_a$ is called the paramagnetic current operator, and $\hat{\gamma}_{ab}$ is known as the diamagnetic current operator as well as the Raman vertex [48,49]. The photon-electron-phonon interaction Hamiltonian is given by the light-field dependence of the electron-phonon interaction, $\mathcal{M}_a^{(1)}[\mathbf{p} + e\mathbf{A}(t)]$ and $\mathcal{M}_{ab}^{(2)}[\mathbf{p} + e\mathbf{A}(t)]$. By expanding electron-phonon matrix elements up to second-order in $\mathbf{A}(t)$, we obtain the photon-electron-phonon (PEP) interaction Hamiltonian $\hat{\mathcal{H}}_{ph-e-p} = \sum_{\mathbf{p}} \hat{\psi}_{\mathbf{p}}^\dagger \hat{\Xi}_{\mathbf{p}} \hat{\psi}_{\mathbf{p}}$, where

$$\hat{\Xi}_{\mathbf{p}} = \sum_{ab} A_a(t) Q_b(t) \left\{ \hat{\Theta}_{ab}^{(1)}(\mathbf{p}) + \sum_c \hat{\Theta}_{abc}^{(2)}(\mathbf{p}) Q_c(t) \right\}$$
$$+ \frac{1}{2} \sum_{abc} A_a(t) A_b(t) Q_c(t)$$
$$\times \left\{ \hat{\Delta}_{abc}^{(1)}(\mathbf{p}) + \sum_d \hat{\Delta}_{abcd}^{(2)}(\mathbf{p}) Q_d(t) \right\}. \tag{11}$$

Having defined all vertex couplings, we are equipped to evaluate the Raman force and the light-induced phonon self-energy. Because the Raman phonon is even under parity, the leading contribution to the Raman force is second order in the light field, which follows

$$\mathcal{F}_a^{(2)}(t) = \sum_{bc} \sum_{\omega_1, \omega_2} e^{i(\omega_1 + \omega_2)t} \sigma_{abc}^{(2)}(\omega_1, \omega_2) E_b(\omega_1) E_c(\omega_2). \tag{12}$$

Similarly, the light-induced instantaneous coupling is given by

$$\mathcal{G}_{ab}^{\text{ins.}}(t) = \sum_{cd} \sum_{\omega_1, \omega_2} e^{i(\omega_1 + \omega_2)t} \Pi_{abcd}^{\text{ins.}}(\omega_1, \omega_2) E_c(\omega_1) E_d(\omega_2). \tag{13}$$

Finally, one can evaluate the light-induced retarded coupling as follows:

$$\mathcal{G}_{ab}^{ret.}(t, t') = \sum_{cd} \sum_{\omega_1, \omega_2} e^{i(\omega_1 + \omega_2)t} \Pi_{abcd}^{ret.}(\omega_1, \omega_2, t - t')$$
$$\times E_c(\omega_1) E_d(\omega_2). \tag{14}$$

Notice that $\Pi_{abcd}^{ret.}(\omega_1, \omega_2, \tau) = \sum_{\omega_3} e^{i\omega_3 \tau} \Pi_{abcd}^{ret.}(\omega_1, \omega_2, \omega_3)$ where ω_3 is the phonon frequency. Response function $\Pi_{abcd}^{\text{ins.}}$ contributes to the instantaneous phonon self-energy since it
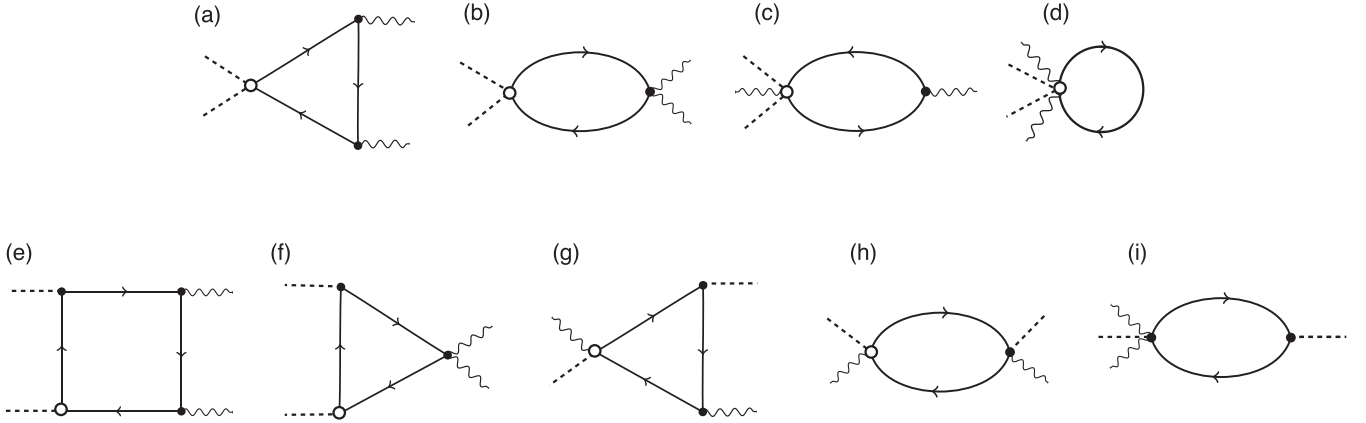
FIG. 2. Feynman diagrams for light-induced phonon self-energy. Diagrams given in (a)–(e) and (f)–(i) for $\mathcal{G}^{\text{ins.}}$ and $\mathcal{G}^{ret.}$ couplings, respectively. Dashed and wave lines represent external phonon and photon fields, respectively. The solid lines represent electron propagators.

originates from the simultaneous coupling of two phonons to electrons. On the other hand, the retarded response function $\Pi^{ret.}_{abcd}$ contains memory effects where the past dynamics of phonons can influence their future motion.

The light-induced rigid displacement directly depends on the displacive Raman force that is the rectified part of the force in a second-order nonlinear process [46]. We consider monochromatic incident light field $\mathbf{E}(t) = E_0\hat{\boldsymbol{\varepsilon}}e^{-i\omega t} + c.c.$ with $\hat{\boldsymbol{\varepsilon}}$ being the linear polarization unit vector. The displacive force is thus given by the rectification process (i.e., $\omega_1 = -\omega_2 = \omega$) that leads to the following time-independent Raman force:

$$\mathcal{F}^{\text{D}}_a = \sum_{bc} \sigma^{(2)}_{abc}(\omega, -\omega)E_b(\omega)E^*_c(\omega). \tag{15}$$

Similarly, the rectified component of the instantaneous phonon-phonon coupling reads

$$\mathcal{G}^{\text{ins.}}_{ab} = \sum_{cd} \Pi^{\text{ins.}}_{abcd}(\omega, -\omega)E_c(\omega)E^*_d(\omega), \tag{16}$$

and the retarded light-induced phonon-phonon coupling follows

$$\mathcal{G}^{ret.}_{ab}(t - t') = \sum_{cd} \Pi^{ret.}_{abcd}(\omega, -\omega, t - t')E_c(\omega)E^*_d(\omega). \tag{17}$$

It is worth highlighting that the second harmonic parts of $\mathcal{G}^{\text{ins.}}_{ab}$ and $\mathcal{G}^{ret.}_{ab} \sim e^{i2\omega t}$ do not contribute noticeably due to its convolution with the slow oscillation of the ion displacement $Q_a \sim e^{i\Omega_0 t}$ since $\omega \gg \Omega_0$. In this regard, the rectified parts of $\mathcal{G}^{\text{ins.}}_{ab}$ and $\mathcal{G}^{ret.}_{ab}$ play the dominant role. Eventually, the phonon equation of motion coherently dressed by the light field is given by

$$\frac{\partial^2 Q_a(t)}{\partial t^2} + \Gamma_p \frac{\partial Q_a(t)}{\partial t} + \Omega^2_0 Q_a(t)$$
$$= \frac{\mathcal{F}^{\text{D}}_a}{\rho} + \frac{1}{\rho}\sum_b \mathcal{G}^{\text{ins.}}_{ab} Q_b(t)$$
$$+ \frac{1}{\rho}\sum_b \int dt' \mathcal{G}^{ret.}_{ab}(t - t')Q_b(t'). \tag{18}$$

We employ a diagrammatic formalism to estimate numerical values of the Raman force [46] and phonon self-energy. Here, the main focus is on the light-induced renormalization and mixing of shear phonons. The Feynman diagrams for the instantaneous and retarded couplings thus are given in Figs. 2(a)–2(d) and Figs. 2(e)–2(i), respectively. To quantitatively analyze the spectral function and the splitting of shear phonons, we microscopically explore the coherent dynamics of shear modes in bilayer graphene in the remaining part of the paper.

III. LIGHT-MATTER AND ELECTRON-PHONON COUPLINGS

Bilayer graphene consists of two single layers of graphene sheets offset from each other in the xy plane. The low-energy quasiparticles follow a two-band Hamiltonian around the corners of the hexagonal Brillouin zone [50]

$$\hat{H}_{\mathbf{p}} = -\frac{1}{2m}\left\{\left(p^2_x - p^2_y\right)\hat{\sigma}_x + 2\tau p_x p_y \hat{\sigma}_y\right\} - \mu\hat{I}. \tag{19}$$

Note that $\boldsymbol{p} = \hbar\boldsymbol{k}$ is the momentum vector, $\tau = \pm$ indicates two K and K′ valley points, the identity matrix $\hat{I}$ and Pauli matrices $\hat{\sigma}_x$ and $\hat{\sigma}_y$ are in the layer pseudospin basis, and μ is the chemical potential. In our convention, the x direction shows a zigzag orientation of the honeycomb lattice [51]. The effective mass is given by $1/2m \approx v^2/|\gamma_1|$ with $v \approx 10^6$ m/s and vertical interlayer hopping energy $\gamma_1 \approx -0.4$ eV [52]. Having the in-plane displacement $\mathbf{Q}^{(\ell)}(\mathbf{r})$ of two layers $\ell = 1, 2$, the shear phonon displacement is the asymmetric component:

$$\mathbf{Q} = \frac{\mathbf{Q}^{(1)} - \mathbf{Q}^{(2)}}{\sqrt{2}}. \tag{20}$$

The shear displacement vector is even under parity $\mathcal{P}$ since $\mathcal{P}\{\mathbf{Q}^{(1)}, \mathbf{Q}^{(2)}\}\mathcal{P}^{-1} = -\{\mathbf{Q}^{(2)}, \mathbf{Q}^{(1)}\}$ leading to $\mathcal{P}\mathbf{Q}\mathcal{P}^{-1} = \mathbf{Q}$. Therefore, the shear mode is a Raman-active but IR-inactive phonon. We consider the coupling of electrons to one and two photons given by $\hat{j}_\alpha = -e\partial_{p_\alpha}\hat{H}_{\mathbf{p}}$ and $\hat{\gamma}_{\alpha\beta} = -e^2\partial_{p_\alpha}\partial_{p_\beta}\hat{H}_{\mathbf{p}}$, respectively. The coupling of electrons to one and two photons

are thus given by

$$(\hat{j}_x, \hat{j}_y) = \frac{e}{m}(p_x\hat{\sigma}_x + \tau p_y\hat{\sigma}_y, -p_y\hat{\sigma}_x + \tau p_x\sigma_y),$$

$$(\hat{\gamma}_{xx} = -\hat{\gamma}_{yy}, \hat{\gamma}_{xy} = \hat{\gamma}_{yx}) = \frac{e^2}{m}(\hat{\sigma}_x, \tau\hat{\sigma}_y). \quad (21)$$

The electron-phonon couplings are obtained using a four-band tight-binding model following the approach developed in Ref. [46] providing the detailed analysis of electron coupling to phonons in bilayer graphene using tight-binding and $\mathbf{k} \cdot \mathbf{p}$ models, see also Refs. [53–55]. Accordingly, the couplings of electrons to shear phonons in the low-energy model read [46]

$$\left(\hat{\mathcal{M}}_x^{(1)}, \hat{\mathcal{M}}_y^{(1)}\right) \approx \mathcal{M}^{(1)}(\tau\hat{\sigma}_y, \hat{\sigma}_x),$$

$$\left(\hat{\mathcal{M}}_{xx}^{(2)} = -\hat{\mathcal{M}}_{yy}^{(2)}, \hat{\mathcal{M}}_{xy}^{(2)} = \hat{\mathcal{M}}_{yx}^{(2)}\right) \approx \mathcal{M}^{(2)}(\hat{\sigma}_x, \tau\hat{\sigma}_y). \quad (22)$$

Electron-phonon coupling can depend on the light field, and this leads to mixed PEP couplings, which are obtained after neglecting electron momentum p [46]

$$\begin{pmatrix} \hat{\Theta}_{xy}^{(1)} = \hat{\Theta}_{yx}^{(1)} \\ \hat{\Theta}_{yy}^{(1)} = -\hat{\Theta}_{xx}^{(1)} \end{pmatrix} \approx -\Theta^{(1)} \begin{pmatrix} \tau\hat{\sigma}_x \\ \hat{\sigma}_y \end{pmatrix}, \quad (23)$$

$$\begin{pmatrix} \Theta_{yyx}^{(2)} = \Theta_{yxy}^{(2)} = \Theta_{xyy}^{(2)} = \Theta_{xxx}^{(2)}/3 \\ \Theta_{xyx}^{(2)} = \Theta_{xxy}^{(2)} = \Theta_{yxx}^{(2)} = \Theta_{yyy}^{(2)}/3 \end{pmatrix} \approx \Theta^{(2)} \begin{pmatrix} \tau\hat{\sigma}_x \\ -\hat{\sigma}_y \end{pmatrix}, \quad (24)$$

$$\begin{pmatrix} \Delta_{xxy}^{(1)} = \Delta_{xyx}^{(1)} = \Delta_{yxx}^{(1)} = \Delta_{yyy}^{(1)}/3 \\ \Delta_{yxy}^{(1)} = \Delta_{yyx}^{(1)} = \Delta_{xyy}^{(1)} = \Delta_{xxx}^{(1)}/3 \end{pmatrix} \approx \Delta^{(1)} \begin{pmatrix} \hat{\sigma}_x \\ \tau\hat{\sigma}_y \end{pmatrix}. \quad (25)$$

The expression for $\Delta_{abcd}^{(2)}$ coupling, representing the coupling of two-photon and two-phonon fields with an electron field, has yet to be specified. However, we can include its contribution using a gauge invariance argument, and therefore there is no need to explicitly calculate $\Delta_{abcd}^{(2)}$ coupling constants. This gauge invariance issue is discussed more explicitly in the following sections.

The values of electron-phonon couplings strength are given in terms of microscopic parameters of the system [46]

$$\mathcal{M}^{(1)} = -\left(\frac{3a_0}{\sqrt{2}b}\right)\left(\frac{\partial\gamma_3}{\partial b}\right) = \left(\frac{3a_0\gamma_3}{\sqrt{2}b^2}\right)\beta_3, \quad (26)$$

$$\mathcal{M}^{(2)} = \left(\frac{3a_0^2}{4b^2}\right)\left(\frac{\partial^2\gamma_3}{\partial b^2}\right) = \left(\frac{3a_0^2\gamma_3}{4b^4}\right)\beta_3(1+\beta_3). \quad (27)$$

where $\gamma_3 \approx 0.3$eV [52] is an interlayer hopping energy corresponding to the hopping of electrons from sublattice A of bottom layer one to sublattice A of the top layer in a Bernal stack bilayer system. The Gruneisen parameter follows $\beta_3 = -\partial \ln \gamma_3/\partial \ln b$. The mixed PEP coupling constants are thus obtained as $\Theta^{(1)} = (ea_0/2\hbar)\mathcal{M}^{(1)}$, $\Delta^{(1)} = (ea_0/2\hbar)^2\mathcal{M}^{(1)}$ and $\Theta^{(2)} = -(ea_0/4\hbar)\mathcal{M}^{(2)}$. Accordingly, the only coupling parameter is β_3. In the second equality of the above relation, we assume the power-law rule $\gamma_3 \sim 1/b^{\beta_3}$ for the dependence of γ_3 on the corresponding bond length $b = \sqrt{a_0^2 + c^2} \approx 0.38$ nm with intralayer carbon-carbon bond length $a_0 = 0.142$ nm and the interlayer distance $c = 0.34$ nm. An analysis based on the density functional calculation estimates the dependence of γ_3 on the bond length as $\partial\gamma_3/\partial b \approx -0.54$ eV/Å [54] and therefore one can obtain the Gruneisen parameter $\beta_3 = -(b/\gamma_3)\partial\gamma_3/\partial b \approx 6.84$. The

vertical hopping derivative $\partial\gamma_1/\partial c$ does not contribute to the leading-order electron-phonon interaction.

IV. NUMERICAL RESULTS AND DISCUSSION

The phonon self-energy terms depend on $\Pi_{abcd}^{\text{ins.}}$ and $\Pi_{abcd}^{ret.}$, which are given in terms of corresponding susceptibilities $\chi_{abcd}^{\text{ins.}}$ and $\chi_{abcd}^{ret.}$ in response to the vector potentials $A_c(\omega_1)$ and $A_d(\omega_2)$. Therefore, we have

$$\Pi_{abcd}^{\text{ins.}}(\omega_1, \omega_2) = -\frac{\chi_{abcd}^{\text{ins.}}(\omega_1, \omega_2)}{(i\omega_1)(i\omega_2)}, \quad (28)$$

$$\Pi_{abcd}^{ret.}(\omega_1, \omega_2, \omega_3) = -\frac{\chi_{abcd}^{ret.}(\omega_1, \omega_2, \omega_3)}{(i\omega_1)(i\omega_2)}, \quad (29)$$

where ω_3 is the phonon frequency. The overall minus sign in the above relations by definition, given in Eq. (8) and Eq. (9). Utilizing Feynman diagrams given in Figs. 2(a)–2(d) and Figs. 2(e)–2(i) we calculate $\chi_{abcd}^{\text{ins.}}$ and $\chi_{abcd}^{ret.}$ response functions, respectively. Before reporting the numerical results, it is necessary to mention that the contribution of the mixed PEP coupling $\Delta_{abcd}^{(2)}$, depicted in the diagram in Fig. 2(d), is frequency independent. One can incorporate this diagram by enforcing the gauge invariance, implying a vanishing system response to a static homogeneous gauge field. Accordingly, we have $\chi_{abcd}^{\text{ins.}}(\omega_1 = 0, \omega_2 = 0) + \chi_{abcd}^{ret.}(\omega_1 = 0, \omega_2 = 0, \omega_3) = 0$ so that the impact of $\Delta_{abcd}^{(2)}$ can be taken into account by subtracting the static value of each diagram.

$$\chi_{abcd}^{ret.}(\omega_1, \omega_2, \omega_3) \rightarrow \chi_{abcd}^{ret.}(\omega_1, \omega_2, \omega_3) - \chi_{abcd}^{ret.}(0, 0, \omega_3),$$

$$\chi_{abcd}^{\text{ins.}}(\omega_1, \omega_2) \rightarrow \chi_{abcd}^{\text{ins.}}(\omega_1, \omega_2) - \chi_{abcd}^{\text{ins.}}(0, 0). \quad (30)$$

The rest of the section summarizes our analytical and numerical results for the light-induced instantaneous and retarded couplings and the resulting renormalization of shear phonon frequency in bilayer graphene. Afterward, we quantitatively analyze the splitting of shear phonon modes and phonon instability which are coherently controllable by altering the incident laser intensity, frequency, and polarization. We also investigate the impact of finite electronic temperature on our numerical results.

A. Light-induced instantaneous self-energy

Light-induced instantaneous phonon self-energy is calculated following the Feynman diagrams depicted in Figs. 2(a)–2(d) employing the effective low-energy description of electrons and the couplings to phonons and photons. For a linearly polarized incident light field $\mathbf{E}(t) = E_0(\hat{\mathbf{x}}\cos\theta + \hat{\mathbf{y}}\sin\theta)e^{-i\omega t} + $ c.c., the symmetry of the system enforces the following constraints for the only nonvanishing tensor elements as $-\Pi_{xxxx}^{\text{ins.}} = -\Pi_{yyyy}^{\text{ins.}} = \Pi_{xxyy}^{\text{ins.}} = \Pi_{yyxx}^{\text{ins.}} = \Pi_{xyxy}^{\text{ins.}} = \Pi_{yxyx}^{\text{ins.}} = \Pi_{xyyx}^{\text{ins.}} = \Pi_{yxxy}^{\text{ins.}} = \Pi^{\text{ins.}}$. In accordance with this symmetry constraint, we find the dependence of $\hat{\mathcal{G}}^{\text{ins.}}$ on the light field polarization angle θ:

$$\hat{\mathcal{G}}^{\text{ins.}} = \Pi^{\text{ins.}}(\bar{\omega}_1, \bar{\omega}_2)E_0^2 \begin{bmatrix} -\cos(2\theta) & \sin(2\theta) \\ \sin(2\theta) & \cos(2\theta) \end{bmatrix}, \quad (31)$$

where $\bar{\omega}_j = \hbar(\omega_j + i\Gamma_e)/|\mu|$ with $\omega_1 = -\omega_2 = \omega$ and $\hbar\Gamma_e$ is the electron scattering rate. The functional dependence of the
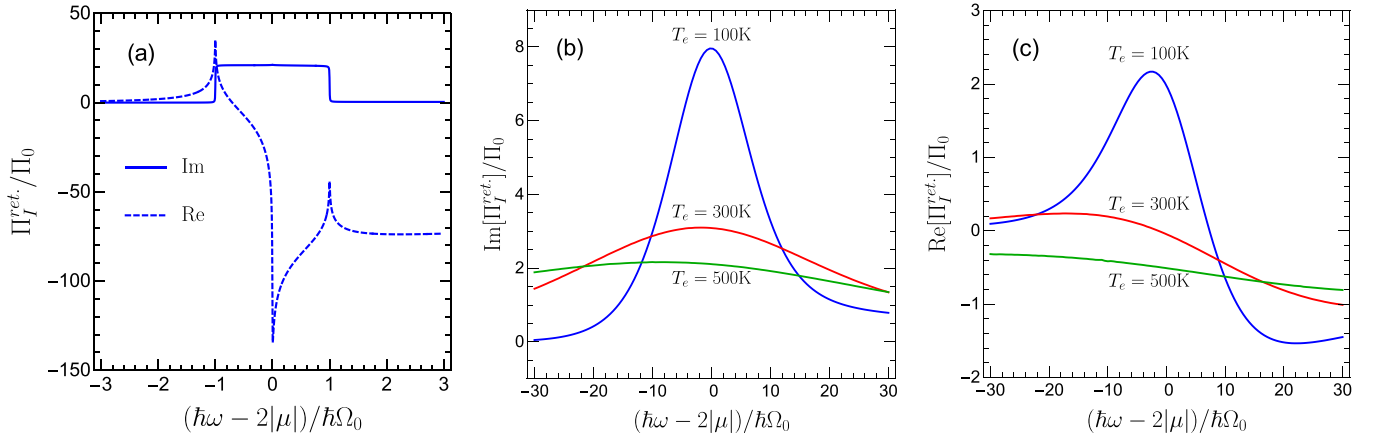
FIG. 3. Light-induced retarded self-energy coupling versus the laser frequency. (a) indicates the imaginary and real parts of $\Pi_I^{ret.}$ versus the incident laser frequency at zero electronic temperature $T_e = 0$ and $\hbar\Gamma_e = 0.001$ meV. (b) and (c), respectively, illustrate the imaginary and real parts of $\Pi_I^{ret.}$ at $\hbar\Gamma_e = 1$ meV and different values of electronic temperature T_e. We set $\mu = 200$ meV, and $\hbar\Omega_0 = 3.9$ meV in this figure.

instantaneous coupling is obtained analytically using the effective low-energy Hamiltonian, and it reads $\Pi^{ins.}(\bar{\omega}_1, \bar{\omega}_2) = \Pi_0^{ins.}\Lambda(\bar{\omega}_1, \bar{\omega}_2)$ with (see Appendix A)

$$\Lambda(\bar{\omega}_1, \bar{\omega}_2) = \left\{ \frac{(\bar{\omega}_1 + 2\bar{\omega}_2)}{\bar{\omega}_2^2(\bar{\omega}_1 + \bar{\omega}_2)} \ln\left[\frac{4 - \bar{\omega}_1^2}{4 - (\omega_1 + \omega_2)^2}\right] \right.$$
$$+ \frac{(\bar{\omega}_2 + 2\bar{\omega}_1)}{\bar{\omega}_1^2(\bar{\omega}_1 + \bar{\omega}_2)} \ln\left[\frac{4 - \bar{\omega}_2^2}{4 - (\bar{\omega}_1 + \bar{\omega}_2)^2}\right]$$
$$\left. - \frac{3}{2\bar{\omega}_1\bar{\omega}_2} \ln\left[1 - \frac{(\omega_1 + \omega_2)^2}{4}\right] \right\}, \quad (32)$$

and the dimensionful constant prefactor reads

$$\Pi_0^{ins.} = \frac{N_f e^2 \mathcal{M}^{(2)}}{4\pi\mu^2}. \quad (33)$$

in which $N_f = 4$ stands for the spin-valley degeneracy. The properties of universal function $\Lambda(\omega_1, \omega_2)$ are explored in Ref. [46] at zero and finite electronic temperature T_e.

B. Light-induced retarded self-energy

For the retarded coupling, we have the Feynman diagrams depicted in Figs. 2(e)–2(i), among which only diagrams shown in Figs. 2(e), 2(h), and 2(i) are nonzero in our effective model analysis. The symmetry of our low-energy model results in constraints for the nonvanishing elements of $\Pi_{abcd}^{ret.}$ as $\Pi_{xxxx}^{ret.} = \Pi_{yyyy}^{ret.}$, $\Pi_{xxyy}^{ret.} = \Pi_{yyxx}^{ret.}$, $\Pi_{xyxy}^{ret.} = \Pi_{yxyx}^{ret.}$, and $\Pi_{xyyx}^{ret.} = \Pi_{yxxy}^{ret.}$. Accordingly, the polarization dependence of the retarded coupling reads

$$\hat{\mathcal{G}}^{ret.}(\Omega) = E_0^2 \Pi_I^{ret.}\hat{I} + E_0^2 \begin{bmatrix} \Pi_Z^{ret.}\cos(2\theta) & \Pi_X^{ret.}\sin(2\theta) \\ \Pi_X^{ret.}\sin(2\theta) & -\Pi_Z^{ret.}\cos(2\theta) \end{bmatrix}, \quad (34)$$

where for a given light field frequency ω and at phonon frequency Ω, we define

$$\Pi_{I,Z}^{ret.}(\omega, -\omega, \Omega) = \frac{\Pi_{xxxx}^{ret.} \pm \Pi_{xxyy}^{ret.}}{2},$$
$$\Pi_X^{ret.}(\omega, -\omega, \Omega) = \frac{\Pi_{xyyx}^{ret.} + \Pi_{xyxy}^{ret.}}{2}. \quad (35)$$

The $+$ and $-$ signs in the above relation refer to $\Pi_I^{ret.}$ and $\Pi_Z^{ret.}$, respectively. The three contributions from three diagrams Figs. 3(a), 3(d), and 3(e) can be collected as follows:

$$\Pi_{\xi=I,Z,X}^{ret.}(\omega_1, \omega_2, \omega_3) = \Pi_0^{ret.}\left\{\Pi_\xi^{square}(\omega_1, \omega_2, \omega_3)\right.$$
$$+ \alpha\left[\Pi_\xi^{bubble-\Theta}(\omega_1, \omega_2, \omega_3)\right.$$
$$\left.\left. + \Pi_\xi^{bubble-\Delta}(\omega_1, \omega_2, \omega_3)\right]\right\}. \quad (36)$$

In the low-energy model, we obtain vanishing contributions for the triangle diagrams shown in Figs. 2(f) and 2(g). The detailed derivation and analytical expressions of the above nonlinear response functions at zero electronic temperature are given in Appendix B. Notice the constant factors

$$\Pi_0^{ret.} = \frac{N_f(e\mathcal{M}^{(1)})^2}{24\pi(\hbar\Gamma_e)\mu^2}, \quad \alpha = \frac{\hbar\Gamma_e}{(18\gamma_0^2/\gamma_1)}. \quad (37)$$

Since $18\gamma_0^2/\gamma_1 \approx 10^2$ eV and $\hbar\Gamma_e$ is usually less than tens of meV, we have $\alpha \ll 1$ for realistic value of scattering rate $\hbar\Gamma_e$. Therefore, we safely neglect the contribution of bubble diagrams relative to the square diagram. Considering the square diagram, our microscopic calculation gives $\Pi_{xxxx}^{ret.} = \Pi_{xxyy}^{ret.}$ and $\Pi_{xyxy}^{ret.} = -\Pi_{xyyx}^{ret.}$. Consequently, we obtain

$$\Pi_I^{ret.} = \Pi_{xxxx}^{ret.} \approx \Pi_I^{square} \quad \text{and} \quad \Pi_Z^{ret.} = \Pi_X^{ret.} = 0. \quad (38)$$

In Fig. 3, we illustrate real and imaginary parts of $\Pi_I^{ret.}$ at zero and finite electronic temperature T_e. At very low temperatures, the imaginary part is finite only in a narrow frequency window close to the interband optical transition gap $2|\mu|$ where the width of the frequency window is given by the shear phonon frequency $2\Omega_0$. The real part of $\Pi_I^{ret.}$ shows logarithmic cusps at optical transition edges for $\hbar\omega = 2\mu$ and $\hbar\omega = 2\mu \pm \hbar\Omega$.

We generalize the zero temperature response function $\Pi_{abcd}(\varepsilon_F, T_e = 0, \dots)$ to finite electronic temperature using the Maldague's formula [46,56], by integrating over the Fermi energy as follows:

$$\Pi_{abcd}|_{\mu, T_e} = \int_{-\infty}^{\infty} dy \frac{\Pi_{abcd}|_{\varepsilon_F \to y, T_e=0}}{4k_B T_e \cosh^2\left(\frac{y-\mu}{2k_B T_e}\right)}. \quad (39)$$
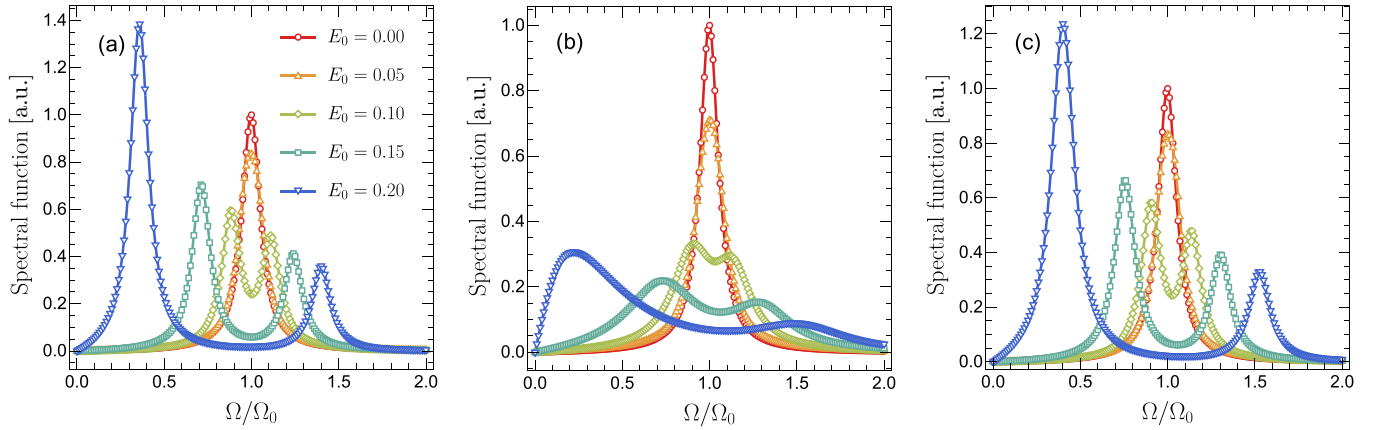
FIG. 4. Adiabatic and nonadiabatic spectral functions of optically dressed shear phonons. (a) and (b) illustrate the results obtained within the adiabatic and nonadiabatic models, respectively. In (c), we depict the spectral function obtained after neglecting the imaginary part of $\Pi_I^{ret.}(\Omega)$. The shear phonons' splitting is depicted at different values of the light field amplitude in the unit of V/nm. The splitting is almost the same in both adiabatic and nonadiabatic models. However, the linewidth and peak values are different in the two models. We set $\mu = 200$ meV, $\hbar\Gamma_e = 5$ meV, $\hbar\Gamma_p = 0.5$ meV, $T_e = 100$ K, $\hbar\Omega_0 = 3.9$ meV, and $\theta = 0$ in this figure.

The electronic temperature can reach thousands of Kelvin due to intense and ultrashort laser pulses [57–61]. The imaginary part of $\Pi_I^{ret.}$ is always positive at zero and finite temperatures. We investigate the impact of the electronic temperature, and the result shows an expected reduction of the response for frequencies in the range $|\hbar\omega - 2|\mu|| < \hbar\Omega_0$ while outside this range, the response function increases by raising the temperature.

C. Light-induced phonon splitting and instability

Performing the Fourier transform of the shear phonon displacement vector $Q_a(t) = \sum_\Omega Q_a(\Omega)e^{-i\Omega t}$ in Eq. (18) leads to the equation of motion into the frequency domain

$$\sum_b \{\mathcal{K}_{ab}(\Omega) - (\Omega^2 + i\Gamma_p\Omega)\delta_{ab}\}Q_b(\Omega) = \frac{\mathcal{F}_a^{\mathrm{D}}}{\rho}, \qquad (40)$$

where the dynamical matrix of shear modes is dressed by the external light field and given by

$$\mathcal{K}_{ab}(\Omega) = \Omega_0^2\delta_{ab} - \frac{\mathcal{G}_{ab}^{\mathrm{ins.}}}{\rho} - \frac{\mathcal{G}_{ab}^{ret.}(\Omega)}{\rho}. \qquad (41)$$

We write the light-induced phonon self-energy term in a compact form in the unit of a characteristic frequency $v_0 = \sqrt{g_0/\rho}$ with $g_0 = \gamma_3(eE_0/b\mu)^2$ and thus the dynamical matrix reads

$$\hat{\mathcal{K}}(\Omega) = \Omega_0^2\hat{I} - v_0^2\begin{bmatrix} K_I + K_Z\cos(2\theta) & K_X\sin(2\theta) \\ K_X\sin(2\theta) & K_I - K_Z\cos(2\theta) \end{bmatrix}, \qquad (42)$$

where for given driving field frequency ω, we have

$$K_I(\Omega) = r_1\Pi_I^{\mathrm{square}}(\omega, -\omega, \Omega),$$
$$K_X = -K_Z = r_0\Lambda(\omega, -\omega). \qquad (43)$$

Notice that $r_0 = 3a_0^2\beta_3(1 + \beta_3)/(4\pi b^2)$ and $r_1 = 3a_0^2\beta_3^2\gamma_3/(4\pi b^2\hbar\Gamma_e)$ are dimensionless parameters. Considering numerical values of γ_3 and β_3 and lattice parameters, we obtain $r_0 \approx 1.738$ and $r_1 \approx 455/(\hbar\Gamma_e[\mathrm{meV}])$.

Utilizing the dynamical matrix, we introduce the phonon Green's function dressed by the light field

$$\hat{D}(\Omega) = [(\Omega^2 + i\Gamma_p\Omega)\hat{I} - \hat{\mathcal{K}}(\Omega)]^{-1}. \qquad (44)$$

Therefore, the spectral function of the shear mode is defined as $\mathcal{A}(\Omega) = -\mathrm{Im}[\mathrm{Tr}[\hat{D}(\Omega)]]/\pi$. By defining $v_0^2\tilde{K}_I(\Omega) = v_0^2K_I(\Omega) + i\Gamma_p\Omega$ and considering $K_X = -K_Z$, we obtain a θ-independent spectral function

$$\mathcal{A}(\Omega) = \frac{2}{\pi}\mathrm{Im}\left[\frac{\Omega_0^2 - \Omega^2 - v_0^2\tilde{K}_I(\Omega)}{\left[\Omega_0^2 - \Omega^2 - v_0^2\tilde{K}_I(\Omega)\right]^2 + v_0^4K_Z^2}\right]. \qquad (45)$$

For displacive Raman force analysis and rigid shear displacement, we only need to know the dynamical matrix at $\Omega = 0$, which corresponds to the adiabatic component of the spectral function. In the adiabatic approximation [62], Green's function is obtained by setting the phonon frequency to zero in the dynamical matrix $\mathcal{K}(\Omega = 0)$:

$$\hat{D}^{\mathrm{ad}}(\Omega) = [(\Omega^2 + i\Gamma_p\Omega)\hat{I} - \hat{\mathcal{K}}(\Omega = 0)]^{-1}. \qquad (46)$$

We calculate the spectral function for both adiabatic and nonadiabatic models, and the results are depicted in Figs. 4(a) and 4(b). Both models predict a splitting of degenerate shear modes due to the impact light field based on the nonlinear Raman mechanism. This comparison shows that the adiabatic approximation nicely predicts the same value for splitting phonon modes in the nonadiabatic formalism. However, the two methods differ for the linewidth and the spectral weight peak value. In particular, in Fig. 4(c), we neglect the imaginary part of $\Pi_I^{ret}(\Omega)$, which results in sharper peaks coinciding with the spectral peaks in the adiabatic model. According to this analysis, we can safely consider an adiabatic approximation by setting $\Omega = 0$ in the dynamical matrix $\hat{\mathcal{K}}(\Omega = 0)$ to discuss the light-induced shear mode splitting and instability at which phonon frequency vanishes. In this case, we diagonalize the adiabatic dynamical matrix and obtain the normal shear phonon modes in a linear superposition of two Cartesian
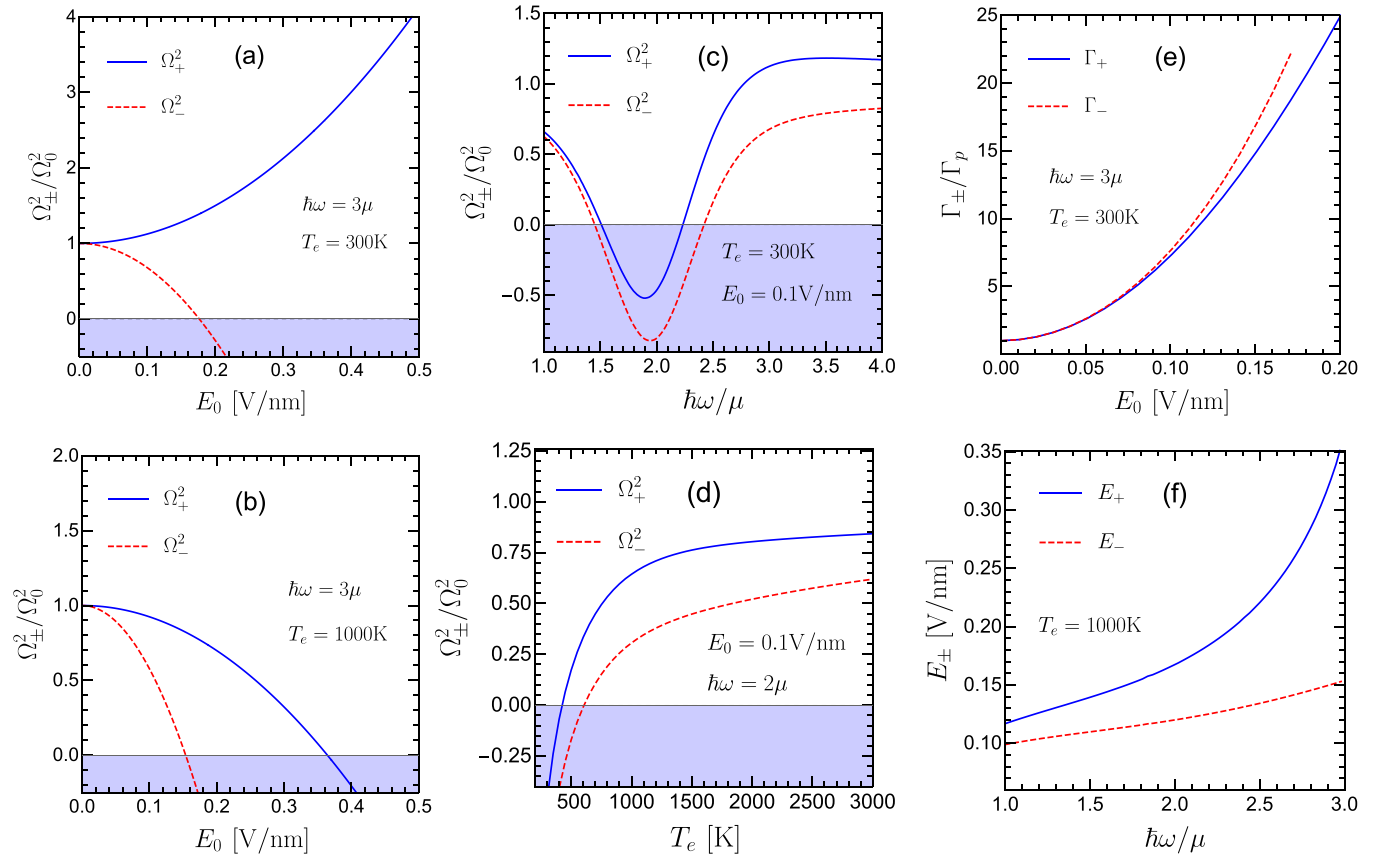
FIG. 5. Light-induced shear phonon splitting and instability. (a) and (b) shows the mode splitting as a function of the light field amplitude at laser frequency $\hbar\omega = 3\mu$ and two different values of electronic temperature. (c) illustrates the frequency dependence of dynamically renormalized shear modes at field amplitude $E_0 = 0.1$ V/nm and $T_e = 300$ K. (d) indicates the shear phonon frequencies versus the electronic temperature at $\hbar\omega = 2\mu$ and $E_0 = 0.1$ V/nm. (e) shows the field dependence of shear phonon linewidth at $\hbar\omega = 3\mu$ and $T_e = 300$ K. (f) manifests the laser frequency dependence of the critical field amplitude at which phonon modes become unstable. We set $\mu = 200$ meV, $\hbar\Gamma_p = 0.1$ meV, $\hbar\Gamma_e = 5$ meV, and $\hbar\Omega_0 = 3.9$ meV in this figure.

modes. Eventually, the normal mode frequencies read

$$\left(\frac{\Omega_\pm}{\Omega_0}\right)^2 = 1 - \xi^2 K_I(0) \pm \xi^2 |K_Z|. \tag{47}$$

Note that $\xi = \nu_0/\Omega_0$ is a dimensionless parameter, and both $K_I(0)$ and K_Z are real numbers. Since $K_I(\Omega)$ is a complex number, its imaginary part induces a field-dependent renormalization of the phonon linewidth that follows

$$\frac{\Gamma_\pm}{\Gamma_p} = 1 + \frac{\nu_0^2}{\Gamma_p \Omega_\pm} \text{Im}[K_I(\Omega_\pm)]. \tag{48}$$

There are some qualitative features in the field-dependent phonon frequency and linewidth: (i) First, our perturbative analysis is primarily valid for small enough ξ; therefore, we have $\Omega_\pm > 0$ in the best validity range of our formalism. However, we can predict the case $\Omega_\pm = 0$ at critical field amplitudes $E_\pm$ for which the shear mode becomes unstable that can facilitate an optically driven structural phase transition of the vdW material via the change in the staking order. (ii) For $K_I(0) = 0$ the splitting of two modes is symmetric and Ω_+ is always nonzero while Ω_- vanishes at $\nu_0 = \Omega_0/\sqrt{|K_Z|}$. (iii) For $|K_Z| \ll |K_I(0)|$, phonons remain degenerate at a larger or smaller frequency relative to Ω_0 for

$K_I(0) < 0$ or $K_I(0) > 0$, respectively. If $K_I(0) > 0$, phonon modes get soften ($\Omega_\pm \to 0$) at a critical field amplitude leading to $\nu_0 = \Omega_0/\sqrt{K_I(0)}$. (iv) Since $\text{Im}[K_I(\Omega_\pm)] > 0$ as shown in Fig. 4(c), we obtain a field-induced broadening of spectral function due to the optically enhanced electron-phonon scattering.

We illustrate the normal mode frequency in Figs. 5(a) and 5(b) as a function of the incident field intensity at two different electronic temperature values manifesting the quadratic dependence on the field amplitude. Figure 5(a) shows that two normal modes conversely evolve where Ω_+ (Ω_-) increases (decreases) by raising the field amplitude E_0. The diverging evolution of two phonon modes' frequency in opposite directions becomes a converging trend with negative renormalization and phonon softening at higher electronic temperatures. This is because $K_I(0)$ enhances by raising the temperature, and thus, it becomes larger than K_Z leading to a converging trend for both $\Omega_\pm$ versus field amplitude E_0. Intriguingly, at a critical value of E_0, we predict a vanishing value for $\Omega_\pm = 0$, and by a further increase of E_0 the phonon frequency becomes imaginary $\Omega_\pm^2 < 0$ indicating a structural instability. As a result of this light-induced instability, atomic layers can easily slide to emerge in other stable or metastable staking orders.

In Fig. 5(c), we show the frequency dependence of the normal modes' energies at room temperature showing the nonmonotonic profile with a strong dependence on the light frequency. In the subgap regime, the phonon frequency drops to zero, then becomes unstable for a range of frequencies around interband transition edge $\hbar\omega = 2\mu$. This is because the real part of $\Pi_I^{ret.}$ is enhanced around $\hbar\omega = 2\mu$ as depicted in Fig. 3(c). Further increasing the laser frequency makes $\Omega_{\pm}^2$ positive and thus stable again. The phonon modes' splitting is stronger at higher laser frequency where $K_I(0)$ becomes less relevant than K_Z. Figure 5(d) depicts the temperature dependence of the normal mode frequencies at the interband transition edge $\hbar\omega = 2|\mu|$ and for a field amplitude $E_0 = 0.1$ V/nm. The real part of $\Pi_I^{ret.}$ is larger at lower temperatures, making both shear modes unstable. By raising the electronic temperature, phonon modes become stable again, and by a further increase in temperature, the renormalization of phonon frequency starts to converge. In addition to the field-dependent phonon frequency, we obtain a robust enhancement of phonon linewidth shown in Fig. 5(e), due to the photon-mediated amplification of electron-phonon scattering. Finally, we investigate the frequency dependence of critical electric fields $E_{\pm}$ at which phonon modes $\Omega_{\pm}$ become unstable. Figure 5(f) shows that the critical fields $E_{\pm}$ increase by raising the laser frequency.

Considering the nonlinear Raman force, one can further manipulate shear phonon renormalization and its impact on rigid shear displacement $\mathbf{Q}_0 = \langle \mathbf{Q}(t) \rangle_{\text{time−average}}$ that reads

$$\mathbf{Q}_0 = -\frac{1}{\rho}\hat{D}(\Omega = 0) \cdot \mathcal{F}^D, \tag{49}$$

where $\mathcal{F}^D$ is the displacive Raman shear force in bilayer graphene [46]. One can transform to the normal mode basis where the dynamical matrix is diagonal for which one finds the rigid shift $Q_0^{\pm} = \mathcal{F}_{\pm}^D/\rho\Omega_{\pm}^2$ for two normal shear phonon modes where $\mathcal{F}_{\pm}^D$ are the displacive Raman force components along the normal mode vibrational directions. For the case of $\theta = 0$, two normal modes Q_+ and Q_- correspond to vibration along x and y direction, respectively. Therefore, the nonlinear Raman force mechanism modulates the light-induced rigid shear displacement via the optically driven renormalization of shear phonon frequency.

Finally, we note that the presented Kubo formalism includes all quantum effects, which can make it a more complex and less intuitive approach. Therefore, it is useful to briefly discuss the light-induced phonon self-energy in a semiclassical method. For example, the instantaneous coupling $\mathcal{G}_{ab}^{\text{ins.}}(t)$ is obtained by taking the expectation value of the two-phonon-electron coupling in the presence of the light field, which can be expressed as $\sum_{\mathbf{k}} \sum_{mn} \mathcal{M}_{ab;mn}^{(2)}(\mathbf{k})\delta\rho_{mn}(\mathbf{k}, t)$, where $M_{ab;mn}^{(2)}$ and $\delta\rho_{mn}$ indicate the two-phonon-electron coupling and the light-induced correction to the density matrix element in the band basis labeled by m and n.

In a semiclassical model, we neglect interband effects and focus only on the intraband density matrix, which is described by the Boltzmann distribution function $f_m(\mathbf{k}, t)$. Therefore, the semiclassical estimation reads $\mathcal{G}_{ab}^{\text{ins.}}(t) \sim \sum_m \mathcal{M}_{ab;mm}^{(2)} \sum_{\mathbf{k}}[f_m(\mathbf{k}, t) - f_m^{\text{FD}}(\mathbf{k})]$, where $f_m^{\text{FD}}(\mathbf{k})$ is the Fermi-Dirac distribution function, and the momentum

dependence of the intraband two-phonon-electron coupling is neglected. Finally, we obtain $\mathcal{G}_{ab}^{\text{ins.}}(t) \sim \mathcal{M}_{ab;cc}^{(2)}\delta n_c(t) + \mathcal{M}_{ab;vv}^{(2)}\delta n_v(t)$, in which $\delta n_c(t)$ and $\delta n_v(t)$ are the photoexcited carrier densities in the conduction (c) and valence (v) bands. Similar to the Raman force discussed in Ref. [46], $\mathcal{G}_{ab}^{\text{ins.}}(t)$ is directly related to the photoexcited carrier density and thus follows a similar frequency profile as shown in Eq. (32). The case of $\mathcal{G}_{ab}^{\text{ins.}}(t, t')$ is more complex and its semiclassical model remains an area for future research.

V. CONCLUSION AND OUTLOOK

In conclusion, we present a complete quantum theory incorporating coherent dressing of electrons and phonons perturbatively. Unlike Floquet theory, the validity of our approach based on Green's function method is for a wide range of driving field frequencies. We apply the formal theory to the coherent optical engineering of shear phonons in bilayer graphene. We obtained strong renormalization of shear phonons' frequency that time-resolved spectroscopy of shear phonons can probe in pump-probe experiments [43,45,63–65]. In particular, we predict a light-induced nonthermal instability of shear vibration modes that can facilitate nondestructive coherent engineering lattice structure in layered materials. The removal of shear mode degeneracy can lead to efficient coherent control of layer stacking and relative lateral motion of graphene sheets by altering the pump laser intensity and polarization. For instance, we can consider the case when one of the normal modes is softened and the other one is hardened due the indirect electron-mediated interaction with the pump laser. This results in a larger shear displacement along the softer mode direction versus the hard one under the influence of a probe laser. Our investigation into light-induced phonon instability offers an approach to significantly manipulate the lattice potential and with an optically stabilized new ground-states structure with different stacking order. Specifically, Fig. 1(c) illustrates the optically induced saddlelike shear potential for which we must also involve the nonlinear phononic terms. The quantitative analysis of the nonlinear shear phononics is a topic for future studies.

Our theory can be applied to other types of phonon modes in heterostructures of layered materials, which involve relative twists of layers. Having a coherent control of shear phonon dynamics provides an optical switching of polar metals, moiré ferroelectrics, and superconductivity in the heterostructures of layered quantum materials [66–74]. For intense incident laser, there is a saturation effect of the light-induced displacement usually observed in experimental measurements of coherent phonon displacement amplitude. This effect is due to the saturation of the optical absorption that can be explained via a saturable absorption process described by the third-order optical conductivity and a nonlinear force fourth-order in the electric field amplitude, e.g., $F \propto EE^*EE^*$. The saturation effect analysis is beyond the scope of this paper and will be discussed elsewhere.

ACKNOWLEDGMENTS

APPENDIX A: INSTANTANEOUS SUSCEPTIBILITY

Considering the contribution of $\Delta_{abcd}^{(2)}$, the instantaneous coupling consists of three contributions

$$\bar{\chi}_{abcd}^{\text{ins.}}(\omega_1, \omega_2) = \bar{\chi}_{abcd}^{\text{triangle}}(\omega_1, \omega_2) + \bar{\chi}_{abcd}^{\text{bubble}-\gamma}(\omega_1, \omega_2)$$
$$+ \bar{\chi}_{abcd}^{\text{bubble}-\Theta}(\omega_1, \omega_2). \tag{A1}$$

In the following sections, we calculate the values of each diagram for the instantaneous susceptibility.

1. Calculation of $\bar{\chi}_{abcd}^{\text{triangle}}$ for the diagram depicted in Fig. 2(a)

The triangle diagram Fig. 2(a) can be written in terms of electronic Green's function $\hat{G}(\mathbf{k}, ik_n)$ and two-phonon-electron matrix element $\hat{\mathcal{M}}_{ab}^{(2)}$ and paramagnetic current operator $\hat{j}_c$, $\hat{j}_d$:

$$\chi_{abcd}(i\omega_{m_1}, i\omega_{m_2}) = \sum_{\mathcal{P}} \frac{1}{S} \sum_{\mathbf{k}} \frac{1}{\beta} \sum_{ik_n} \text{Tr}\big[\hat{\mathcal{M}}_{ab}^{(2)}(\mathbf{k}) \hat{G}(\mathbf{k}, ik_n)$$
$$\times \hat{j}_c(\mathbf{k}) \hat{G}(\mathbf{k}, ik_n + i\omega_{m_1}) \hat{j}_d(\mathbf{k}) \hat{G}(\mathbf{k}, ik_n$$
$$+ i\omega_{m_1} + i\omega_{m_2}) \big], \tag{A2}$$

where the trace operator $\text{Tr}[\dots]$ sum over all spinor degree of freedom, $\beta = 1/k_B T_e$, ik_n ($i\omega_m$) stands for the fermionic (bosonic) Matsubara frequency. The intrinsic permutation symmetry is enforced by $\sum_{\mathcal{P}}$ for the exchange of photon frequencies and corresponding tensorial index: $(c, m_1) \leftrightarrow (d, m_2)$. From now on, we adopt a shorthand notation $ik_n \rightarrow n$ and $i\omega_m \rightarrow m$ for the sake of simplicity. The electronic Green's function is given as follows:

$$\hat{G}(\mathbf{k}, ik_n) = [ik_n - \hat{H}_{\mathbf{k}}]^{-1}. \tag{A3}$$

Because of the inversion symmetry, the response tensor elements with odd Cartesian index x and y vanishes $\chi_{xxxy} = \chi_{xxyx}, = \chi_{yxxy} = \chi_{yyyx} = \chi_{xyxx} = \chi_{xyyy} = \chi_{yxxx} = \chi_{yxyy} = 0$. This symmetry consideration is confirmed by an explicit calculation based on the low-energy two-band model. The remaining tensor elements are also related to each other due to the rotation symmetry of the system:

$$-\chi_{xxxx} = -\chi_{yyyy} = \chi_{xxyy} = \chi_{yyxx} = \chi_{xyyx}$$
$$= \chi_{xyxy} = \chi_{yxyx} = \chi_{yxxy} = \chi_1. \tag{A4}$$

After performing the integration on the azimuthal angle of electronic wave vector $\mathbf{k}$ and using the low-energy dispersion $\epsilon_{\mathbf{k}} = \hbar^2 k^2/2m$ and $k\,dk = (m/\hbar^2)d\epsilon$ we find

$$\chi_1(m_1, m_2) = \left(\frac{N_f \mathcal{M}^{(2)}}{2\pi}\right) \left(\frac{e}{m}\right)^2 \left(\frac{m}{\hbar^2}\right) \int_0^\infty d\epsilon \frac{1}{\beta} \sum_n \frac{8\epsilon^2 \xi(n)(2\epsilon^2 - \xi(m_1+n)^2 - \xi(m_2+n)^2)\xi(m_1+m_2+n)}{(\epsilon^2 - \xi(n)^2)(\epsilon^2 - \xi(m_1+n)^2)(\epsilon^2 - \xi(m_2+n)^2)(\epsilon^2 - \xi(m_1+m_2+n)^2)}, \tag{A5}$$

where $\xi(n) = \mu + n$. After performing Matsubara summation, integrating over ϵ at zero temperature and analytical continuation $m_i \rightarrow \omega_i + i0^+$, we find

$$\chi_1(\omega_1, \omega_2) = \frac{N_f \mathcal{M}^{(2)} e^2}{4\pi \hbar^2} \big\{ A_1 \ln\big[4\epsilon^2 - \omega_1^2\big] + A_2 \ln\big[4\epsilon^2 - \omega_2^2\big] + A_3 \ln\big[4\epsilon^2 - (\omega_1+\omega_2)^2\big] \big\}_{\epsilon \rightarrow \mu}^{\epsilon \rightarrow \infty}. \tag{A6}$$

Here, by ω_i we mean $\hbar\omega_i + i0^+$ and A_i factors read

$$A_1 = \frac{\omega_1(\omega_1 + 2\omega_2)}{\omega_2(\omega_1 + \omega_2)}, \quad A_2 = \frac{\omega_2(\omega_2 + 2\omega_1)}{\omega_1(\omega_1 + \omega_2)}, \quad A_3 = -1 - (A_1 + A_2). \tag{A7}$$

By subtracting the zero-frequency contribution and after some simplifications, we find

$$\chi_1(\omega_1, \omega_2) - \chi_1(0, 0) = \frac{N_f \mathcal{M}^{(2)} e^2}{4\pi \hbar^2} \left\{ A_1 \ln\left[\frac{4\epsilon^2 - \omega_1^2}{4\epsilon^2 - (\omega_1 + \omega_2)^2}\right] + A_2 \ln\left[\frac{4\epsilon^2 - \omega_2^2}{4\epsilon^2 - (\omega_1 + \omega_2)^2}\right] - \ln\left[\frac{4\epsilon^2 - (\omega_1 + \omega_2)^2}{4\epsilon^2}\right] \right\}_{\epsilon \rightarrow \mu}^{\epsilon \rightarrow \infty}. \tag{A8}$$

Eventually, we obtain $\bar{\chi}_1^{\text{triangle}}(\omega_1, \omega_2) = \chi_1(\omega_1, \omega_2) - \chi_1(0, 0)$ as follows:

$$\bar{\chi}_1^{\text{triangle}}(\omega_1, \omega_2) = \frac{N_f \mathcal{M}^{(2)} e^2}{4\pi \hbar^2} \left\{ \ln\left[1 - \frac{(\omega_1 + \omega_2)^2}{4\mu^2}\right] - A_1 \ln\left[\frac{4\mu^2 - \omega_1^2}{4\mu^2 - (\omega_1 + \omega_2)^2}\right] - A_2 \ln\left[\frac{4\mu^2 - \omega_2^2}{4\mu^2 - (\omega_1 + \omega_2)^2}\right] \right\}. \tag{A9}$$

2. Calculation of $\bar{\chi}_{abcd}^{\text{bubble}-\gamma}$ for the diagram depicted in Fig. 2(b)

The bubble diagram Fig. 2(b) can be written in terms of electronic Green's function $\hat{G}(\mathbf{k}, n)$, electron-phonon matrix element $\hat{\mathcal{M}}_{ab}^{(2)}$ and the Raman vertex $\hat{\gamma}_{cd}$:

$$\chi_{abcd}(m_1, m_2) = -\frac{1}{S} \sum_{\mathbf{k}} \frac{1}{\beta} \sum_n \text{Tr}\big[\hat{\mathcal{M}}_{ab}^{(2)}(\mathbf{k}) \hat{G}(\mathbf{k}, n) \hat{\gamma}_{cd}(\mathbf{k}) \hat{G}(\mathbf{k}, n + m_1 + m_2) \big]. \tag{A10}$$

The overall minus sign originates from the standard rules of Feynman diagrams [48], also see Ref. [75]. Similar to the previous diagram, we have $\chi_{xxxy} = \chi_{xxyx} = \chi_{yxyx} = \chi_{yyyx} = \chi_{xyxx} = \chi_{xyyy} = \chi_{yxxx} = \chi_{yxyy} = 0$. The other nonvanishing tensor elements

read

$$-\chi_{xxxx} = -\chi_{yyyy} = \chi_{xxyy} = \chi_{yyxx} = \chi_{xyyx} = \chi_{xyxy} = \chi_{yxyx} = \chi_{yxxy} = \chi_2. \tag{A11}$$

After performing the integration on the azimuthal angle of electronic wave vector $\mathbf{k}$ and using the low-energy dispersion $\epsilon_{\mathbf{k}} = \hbar^2 k^2/2m$ and $kdk = (m/\hbar^2)d\epsilon$ we find

$$\chi_2(m_1, m_2) = N_f \frac{m}{\hbar^2} \frac{e^2 \mathcal{M}^{(2)}}{2\pi m} \int_0^\infty d\epsilon \frac{1}{\beta} \sum_n \frac{2\xi(n)\xi(m_1 + m_2 + n)}{(\epsilon^2 - \xi(n)^2)(\epsilon^2 - \xi(m_1 + m_2 + n)^2)}. \tag{A12}$$

After performing the summation on the Matsubara frequency n and subtracting the zero-frequency contribution, we find

$$\chi_2(\omega_1, \omega_2) - \chi_2(0,0) = -\frac{N_f \mathcal{M}^{(2)} e^2}{8\pi \hbar^2} \left\{ \ln\left[\frac{4\epsilon^2 - (\omega_1 + \omega_2)^2}{4\epsilon^2} \right] \right\}_{\epsilon \to \mu}^{\epsilon \to \infty}. \tag{A13}$$

Finally, we obtain

$$\bar{\chi}_2^{\text{bubble}-\gamma}(\omega_1, \omega_2) = \frac{N_f \mathcal{M}^{(2)} e^2}{8\pi \hbar^2} \ln\left[1 - \frac{(\omega_1 + \omega_2)^2}{4\mu^2} \right]. \tag{A14}$$

3. Calculation of $\bar{\chi}_{abcd}^{\text{bubble}-\Theta}$ for the diagram depicted in Fig. 2(c)

The bubble diagram Fig. 2(c) can be written in terms of electronic Green's function $\hat{G}(\mathbf{k}, n)$, photon-electron-phonon vertex $\hat{\Theta}_{abc}^{(2)}$ and the paramagnetic current $\hat{j}_d$. Considering the permutation symmetry, we have

$$\chi_{abcd}(m_1, m_2) = -\frac{1}{2S} \sum_{\mathbf{k}} \frac{1}{\beta} \sum_n \text{Tr}\left[\hat{\Theta}_{abc}^{(2)}(\mathbf{k}) \hat{G}(\mathbf{k}, n) \hat{j}_d(\mathbf{k}) \hat{G}(\mathbf{k}, n + m_2) \right]$$

$$- \frac{1}{2S} \sum_{\mathbf{k}} \frac{1}{\beta} \sum_n \text{Tr}\left[\hat{\Theta}_{abd}^{(2)}(\mathbf{k}) \hat{G}(\mathbf{k}, n) \hat{j}_c(\mathbf{k}) \hat{G}(\mathbf{k}, n + m_1) \right]. \tag{A15}$$

Using the isotropic approximation for the PEP vertex given in Eq. (6) and after performing the integration on the azimuthal angle of electronic wave vector $\mathbf{k}$, we obtain a vanishing result for all tensor elements. Therefore, within our low-energy model analysis, the mix of photon-electron-phonon coupling does not contribute to the Raman force:

$$\bar{\chi}_{abcd}^{\text{bubble}-\Theta}(\omega_1, \omega_2) = 0. \tag{A16}$$

4. Sum of all diagrams for the instantaneous coupling

Similar to the Raman force case, we obtain $\bar{\chi}^{\text{ins.}}(\omega_1, \omega_2) = \bar{\chi}_1(\omega_1, \omega_2) + \bar{\chi}_2(\omega_1, \omega_2)$. One main difference is that instead of $\mathcal{M}^{(1)}$ we have $\mathcal{M}^{(2)}$:

$$\bar{\chi}_{xxxx}^{\text{ins.}}(\omega_1, \omega_2) = \frac{N_f \mathcal{M}^{(2)} e^2}{4\pi \hbar^2} \left\{ \frac{3}{2} \ln\left[1 - \frac{(\omega_1 + \omega_2)^2}{4\mu^2} \right] - \frac{\omega_1(\omega_1 + 2\omega_2)}{\omega_2(\omega_1 + \omega_2)} \ln\left[\frac{4\mu^2 - \omega_1^2}{4\mu^2 - (\omega_1 + \omega_2)^2} \right] \right.$$

$$\left. - \frac{\omega_2(\omega_2 + 2\omega_1)}{\omega_1(\omega_1 + \omega_2)} \ln\left[\frac{4\mu^2 - \omega_2^2}{4\mu^2 - (\omega_1 + \omega_2)^2} \right] \right\}. \tag{A17}$$

Finally, by considering a linear polarized incident electric field $\mathbf{E}(t) = E_0(\hat{\mathbf{x}} \cos\theta + \hat{\mathbf{y}} \sin\theta) e^{-i\omega t} + c.c$, we find

$$\hat{\mathcal{G}}^{\text{ins.}}(\omega_1, \omega_2) = \Pi_{xxxx}^{\text{ins.}}(\omega_1, \omega_2) E_0^2 \begin{bmatrix} -\cos(2\theta) & \sin(2\theta) \\ \sin(2\theta) & \cos(2\theta) \end{bmatrix}. \tag{A18}$$

The rectified part of $\hat{\mathcal{G}}^{\text{ins.}}$ is obtain after setting $\omega_1 = \hbar(\omega + i0^+)$ and $\omega_2 = \hbar(-\omega + i0^+)$ where ω is the incident laser frequency and Γ_e stands for the effective scattering rate of electrons.

APPENDIX B: RETARDED SUSCEPTIBILITY

The retarded coupling is given in terms of five different diagrams

$$\bar{\chi}_{abcd}^{ret.}(\omega_1, \omega_2, \omega_3) = \bar{\chi}_{abcd}^{\text{square}}(\omega_1, \omega_2, \omega_3) + \bar{\chi}_{abcd}^{\text{triangle}-\gamma}(\omega_1, \omega_2, \omega_3) + \bar{\chi}_{abcd}^{\text{triangle}-\Theta}(\omega_1, \omega_2, \omega_3)$$

$$+ \bar{\chi}_{abcd}^{\text{bubble}-\Theta}(\omega_1, \omega_2, \omega_3) + \bar{\chi}_{abcd}^{\text{bubble}-\Delta}(\omega_1, \omega_2, \omega_3). \tag{B1}$$

In the following, we calculate the explicit expression of each contribution using standard Kubo's formalism at zero electronic temperature.

1. Calculation of $\bar{\chi}_{abcd}^{\text{square}}$ for the diagram depicted in Fig. 2(e)

The square diagram Fig. 2(e) can be written in terms of electronic Green's function $\hat{G}(\mathbf{k}, ik_n)$ and two-phonon-electron matrix element $\hat{\mathcal{M}}_a^{(1)}$, $\hat{\mathcal{M}}_b^{(1)}$ and paramagnetic current operators $\hat{j}_c$, $\hat{j}_d$:

$$\chi_{abcd}(m_1, m_2, m_3) = \frac{1}{3!} \sum_{\mathcal{P}} \frac{1}{S} \sum_{\mathbf{k}} \frac{1}{\beta} \sum_n \text{Tr}\big[\hat{\mathcal{M}}_a^{(1)}(\mathbf{k})\hat{G}(\mathbf{k}, n)\hat{\mathcal{M}}_b^{(1)}(\mathbf{k})\hat{G}(\mathbf{k}, n+m_3)\hat{j}_c(\mathbf{k})\hat{G}(\mathbf{k}, n+m_3+m_1)$$
$$\times \hat{j}_d(\mathbf{k})\hat{G}(\mathbf{k}, n+m_3+m_1+m_2)\big]. \tag{B2}$$

Note that $\sum_{\mathcal{P}}$ stands to ensure the intrinsic permutation symmetry. Because of the inversion symmetry, the response tensor elements with odd Cartesian index x and y vanishes $\chi_{xxxy} = \chi_{xyxx} = \chi_{yyxy} = \chi_{yyyx} = \chi_{xyxx} = \chi_{xyyy} = \chi_{yxxx} = \chi_{yxyy} = 0$. Accordingly, there are only four independent tensor elements

$$\chi_{xxxx} = \chi_{yyyy}, \quad \chi_{xxyy} = \chi_{yyxx}, \quad \chi_{xyxy} = \chi_{yxyx}, \quad \chi_{xyyx} = \chi_{yxxy}. \tag{B3}$$

By performing a straightforward algebra similar to what was discussed in the previous section, one can obtain the four nonvanishing tensor elements in the following form:

$$\chi_{xxxx}(\omega_1, \omega_2, \omega_3) = \chi_{xxyy}(\omega_1, \omega_2, \omega_3) = \frac{N_f}{24\pi}\left(\frac{e\mathcal{M}^{(1)}}{\hbar}\right)^2 \left\{ -\frac{4\omega_1\omega_2\big(\omega_1^2 + (\omega_2+\omega_3)\omega_1 + \omega_3(\omega_2+\omega_3)\big)}{(\omega_1+\omega_2)\omega_3(\omega_1+\omega_3)(\omega_2+\omega_3)(\omega_1+\omega_2+\omega_3)} \ln\left[\frac{2|\mu|-\omega_1}{2|\mu|+\omega_1}\right] \right.$$
$$-\frac{4\omega_1\omega_2\big(\omega_2^2 + \omega_3\omega_2 + \omega_3^2 + \omega_1(\omega_2+\omega_3)\big)}{(\omega_1+\omega_2)\omega_3(\omega_1+\omega_3)(\omega_2+\omega_3)(\omega_1+\omega_2+\omega_3)} \ln\left[\frac{2|\mu|-\omega_2}{2|\mu|+\omega_2}\right]$$
$$+\frac{4\omega_3\big((\omega_2+\omega_3)\omega_1^2 + (\omega_2^2+3\omega_3\omega_2+\omega_3^2)\omega_1 + \omega_2\omega_3(\omega_2+\omega_3)\big)}{\omega_1\omega_2(\omega_1+\omega_2)(\omega_1+\omega_3)(\omega_2+\omega_3)} \ln\left[\frac{2|\mu|-\omega_3}{2|\mu|+\omega_3}\right]$$
$$-\frac{4(\omega_1+\omega_3)\big(\omega_1(\omega_3-\omega_2)+\omega_3(\omega_2+\omega_3)\big)}{\omega_1\omega_2\omega_3(\omega_1+\omega_2+\omega_3)} \ln\left[\frac{2|\mu|-\omega_1-\omega_3}{2|\mu|+\omega_1+\omega_3}\right]$$
$$-\frac{4(\omega_2+\omega_3)\big(\omega_1(\omega_3-\omega_2)+\omega_3(\omega_2+\omega_3)\big)}{\omega_1\omega_2\omega_3(\omega_1+\omega_2+\omega_3)} \ln\left[\frac{2|\mu|-\omega_2-\omega_3}{2|\mu|+\omega_2+\omega_3}\right]$$
$$\left. +\frac{4\omega_3\big(\omega_1^3 + 2(\omega_2+\omega_3)\omega_1^2 + (2\omega_2^2+3\omega_3\omega_2+\omega_3^2)\omega_1 + \omega_2(\omega_2+\omega_3)^2\big)}{\omega_1\omega_2(\omega_1+\omega_2)(\omega_1+\omega_3)(\omega_2+\omega_3)} \ln\left[\frac{2|\mu|-\omega_1-\omega_2-\omega_3}{2|\mu|+\omega_1+\omega_2+\omega_3}\right] \right\}, \tag{B4}$$

and

$$\chi_{xyxy}(\omega_1, \omega_2, \omega_3) = -\chi_{xyyx}(\omega_1, \omega_2, \omega_3) = \frac{N_f}{24\pi}\left(\frac{e\mathcal{M}^{(1)}}{\hbar}\right)^2 \left\{ \frac{4\omega_1(\omega_1+\omega_2+2\omega_3)}{\omega_2(\omega_1+\omega_2+\omega_3)\omega_3} \ln\left[\frac{2|\mu|-\omega_1}{2|\mu|+\omega_1}\right] \right.$$
$$-\frac{4\omega_2(\omega_1+\omega_2+2\omega_3)}{\omega_1(\omega_1+\omega_2+\omega_3)\omega_3} \ln\left[\frac{2|\mu|-\omega_2}{2|\mu|+\omega_2}\right] + \frac{4(\omega_1-\omega_2)\omega_3}{\omega_1\omega_2(\omega_1+\omega_2+\omega_3)} \ln\left[\frac{2|\mu|-\omega_3}{2|\mu|+\omega_3}\right]$$
$$-\frac{4(\omega_1^2-\omega_2^2)(\omega_1+\omega_2+2\omega_3)}{\omega_1\omega_2(\omega_1+\omega_2+\omega_3)\omega_3} \ln\left[\frac{2|\mu|-\omega_1-\omega_2}{2|\mu|+\omega_1+\omega_2}\right]$$
$$-\frac{4(\omega_1+\omega_3)\big(\omega_1^2+(\omega_2+\omega_3)\omega_1-\omega_2\omega_3\big)}{\omega_1\omega_2(\omega_1+\omega_2+\omega_3)\omega_3} \ln\left[\frac{2|\mu|-\omega_1-\omega_3}{2|\mu|+\omega_1+\omega_3}\right]$$
$$+\frac{4(\omega_2+\omega_3)\big(\omega_1(\omega_2-\omega_3)+\omega_2(\omega_2+\omega_3)\big)}{\omega_1\omega_2(\omega_1+\omega_2+\omega_3)\omega_3} \ln\left[\frac{2|\mu|-\omega_2-\omega_3}{2|\mu|+\omega_2+\omega_3}\right]$$
$$\left. +\frac{4(\omega_1-\omega_2)(\omega_1+\omega_2+\omega_3)}{\omega_1\omega_2\omega_3} \ln\left[\frac{2|\mu|-\omega_1-\omega_2-\omega_3}{2|\mu|+\omega_1+\omega_2+\omega_3}\right] \right\}. \tag{B5}$$

For the shorthand notation we adapt ω_i for $\hbar(\omega_i + i0^+)$ in the above relations.

2. Calculation of $\bar{\chi}_{abcd}^{\text{triangle}-\gamma}$ for the diagram depicted in Fig. 2(f)

The triangle diagram Fig. 2(f) can be written in terms of electronic Green's function $\hat{G}(\mathbf{k}, ik_n)$ and electron-phonon matrix element $\hat{\mathcal{M}}_a^{(1)}$, $\hat{\mathcal{M}}_b^{(1)}$ and diamagnetic current operator $\hat{\gamma}_{cd}$:

$$\chi_{abcd}(m_1, m_2, m_3) = -\sum_{\mathcal{P}} \frac{1}{S} \sum_{\mathbf{k}} \frac{1}{\beta} \sum_n \text{Tr}\big[\hat{\mathcal{M}}_a^{(1)}(\mathbf{k})\hat{G}(\mathbf{k}, n)\hat{\mathcal{M}}_b^{(1)}(\mathbf{k})\hat{G}(\mathbf{k}, n+m_1)\hat{\gamma}_{cd}(\mathbf{k})\hat{G}(\mathbf{k}, n+m_1+m_2+m_3)\big] \tag{B6}$$

Using the isotropic approximation model Hamiltonian and after performing the integration on the azimuthal angle of electronic wave vector $\mathbf{k}$, we obtain a vanishing result for all tensor elements. Therefore, within our low-energy model analysis, we have

$$\chi_{abcd}^{\text{triangle}-\gamma}(\omega_1, \omega_2, \omega_3) = 0. \tag{B7}$$

3. Calculation of $\bar{\chi}_{abcd}^{\text{triangle}-\Theta}$ for the diagram depicted in Fig. 2(g)

The triangle diagram Fig. 2(g) can be written in terms of electronic Green's function $\hat{G}(\mathbf{k}, ik_n)$ and photon-electron-phonon matrix element $\hat{\Theta}_{ac}^{(1)}$, electron-phonon matrix element $\hat{\mathcal{M}}_b^{(1)}$, and paramagnetic current operator $\hat{j}_d$:

$$\chi_{abcd}(m_1, m_2, m_3) = \sum_{\mathcal{P}} \frac{1}{2S} \sum_{\mathbf{k}} \frac{1}{\beta} \sum_n \text{Tr}\left[\hat{\Theta}_{ac}^{(1)}(\mathbf{k})\hat{G}(\mathbf{k}, n)\hat{\mathcal{M}}_b^{(1)}(\mathbf{k})\hat{G}(\mathbf{k}, n+m_1)\hat{j}_d(\mathbf{k})\hat{G}(\mathbf{k}, n+m_1+m_3)\right]$$

$$+ \sum_{\mathcal{P}} \frac{1}{2S} \sum_{\mathbf{k}} \frac{1}{\beta} \sum_n \text{Tr}\left[\hat{\Theta}_{ad}^{(1)}(\mathbf{k})\hat{G}(\mathbf{k}, n)\hat{\mathcal{M}}_b^{(1)}(\mathbf{k})\hat{G}(\mathbf{k}, n+m_1)\hat{j}_c(\mathbf{k})\hat{G}(\mathbf{k}, n+m_1+m_2)\right]. \tag{B8}$$

Using the isotropic approximation model Hamiltonian and after performing the integration on the azimuthal angle of electronic wave vector $\mathbf{k}$, we obtain a vanishing result for all tensor elements. Therefore, within our low-energy model analysis, we have

$$\chi_{abcd}^{\text{triangle}-\Theta}(\omega_1, \omega_2, \omega_3) = 0. \tag{B9}$$

4. Calculation of $\bar{\chi}_{abcd}^{\text{bubble}-\Theta}$ for the diagram depicted in Fig. 2(h)

The triangle diagram Fig. 2(h) can be written in terms of electronic Green's function $\hat{G}(\mathbf{k}, ik_n)$ and photon-electron-phonon matrix element $\hat{\Theta}_{ac}^{(1)}$:

$$\chi_{abcd}(m_1, m_2, m_3) = \sum_{\mathcal{P}} \frac{1}{2S} \sum_{\mathbf{k}} \frac{1}{\beta} \sum_n \text{Tr}\left[\hat{\Theta}_{ac}^{(1)}(\mathbf{k})\hat{G}(\mathbf{k}, n)\hat{\Theta}_{bd}^{(1)}(\mathbf{k})\hat{G}(\mathbf{k}, n+m_2+m_3)\right]$$

$$+ \sum_{\mathcal{P}} \frac{1}{2S} \sum_{\mathbf{k}} \frac{1}{\beta} \sum_n \text{Tr}\left[\hat{\Theta}_{ad}^{(1)}(\mathbf{k})\hat{G}(\mathbf{k}, n)\hat{\Theta}_{bc}^{(1)}(\mathbf{k})\hat{G}(\mathbf{k}, n+m_1+m_3)\right]. \tag{B10}$$

Similar to the square diagram the only nonvanishing tensor elements are given by $\chi_{xxxx} = \chi_{yyyy}$, $\chi_{xxyy} = \chi_{yyxx}$, $\chi_{xyxy} = \chi_{yxyx}$, $\chi_{xyyx} = \chi_{yxxy}$. The straightforward algebra similar to what was discussed earlier, one can obtain the four nonvanishing tensor elements in the following form:

$$\bar{\chi}_{xxxx}(\omega_1, \omega_2, \omega_3) = C_{\Theta}\left\{\ln\left[1 - \frac{(\omega_1 + \omega_2)^2}{4\mu^2}\right] + \ln\left[1 - \frac{(\omega_1 + \omega_3)^2}{4\mu^2}\right] + \ln\left[1 - \frac{(\omega_2 + \omega_3)^2}{4\mu^2}\right]\right\}, \tag{B11}$$

$$\bar{\chi}_{xxyy}(\omega_1, \omega_2, \omega_3) = C_{\Theta}\left\{-\ln\left[1 - \frac{(\omega_1 + \omega_2)^2}{4\mu^2}\right] + \ln\left[1 - \frac{(\omega_1 + \omega_3)^2}{4\mu^2}\right] + \ln\left[1 - \frac{(\omega_2 + \omega_3)^2}{4\mu^2}\right]\right\}, \tag{B12}$$

$$\bar{\chi}_{xyyx}(\omega_1, \omega_2, \omega_3) = C_{\Theta}\left\{\ln\left[1 - \frac{(\omega_1 + \omega_2)^2}{4\mu^2}\right] - \ln\left[1 - \frac{(\omega_1 + \omega_3)^2}{4\mu^2}\right] + \ln\left[1 - \frac{(\omega_2 + \omega_3)^2}{4\mu^2}\right]\right\}, \tag{B13}$$

$$\bar{\chi}_{xyxy}(\omega_1, \omega_2, \omega_3) = C_{\Theta}\left\{\ln\left[1 - \frac{(\omega_1 + \omega_2)^2}{4\mu^2}\right] + \ln\left[1 - \frac{(\omega_1 + \omega_3)^2}{4\mu^2}\right] - \ln\left[1 - \frac{(\omega_2 + \omega_3)^2}{4\mu^2}\right]\right\}. \tag{B14}$$

where

$$C_{\Theta} = \frac{N_f m [\Theta^{(1)}]^2}{24\pi \hbar^2}. \tag{B15}$$

5. Calculation of $\bar{\chi}_{abcd}^{\text{bubble}-\Delta}$ for the diagram depicted in Fig. 2(i)

The triangle diagram Fig. 2(i) can be written in terms of electronic Green's function $\hat{G}(\mathbf{k}, ik_n)$ and photon-electron-phonon matrix element $\hat{\Delta}_{acd}^{(1)}$ and electron-phonon matrix element $\hat{\mathcal{M}}_b^{(1)}$:

$$\chi_{5,abcd}(m_1, m_2, m_3) = \sum_{\mathcal{P}} \frac{1}{2S} \sum_{\mathbf{k}} \frac{1}{\beta} \sum_n \text{Tr}\left[\hat{\Delta}_{acd}^{(1)}(\mathbf{k})\hat{G}(\mathbf{k}, n)\hat{\mathcal{M}}_b^{(1)}(\mathbf{k})\hat{G}(\mathbf{k}, n+m_3)\right] \tag{B16}$$

Similar to the square diagram the only nonvanishing tensor elements are given by $\chi_{xxxx} = \chi_{yyyy}$, $\chi_{xxyy} = \chi_{yyxx}$, $\chi_{xyxy} = \chi_{yxyx}$, $\chi_{xyyx} = \chi_{yxxy}$. The straightforward algebra similar to what was discussed earlier, one can obtain the four nonvanishing tensor elements in the following form:

$$\bar{\chi}_{xxxx}(\omega_1, \omega_2, \omega_3) = -\frac{3C_{\Delta}}{2}\left\{\ln\left[1 - \frac{\omega_1^2}{4\mu^2}\right] + \ln\left[1 - \frac{\omega_2^2}{4\mu^2}\right] + \ln\left[1 - \frac{\omega_3^2}{4\mu^2}\right]\right\}, \tag{B17}$$

$$\bar{\chi}_{xxyy}(\omega_1, \omega_2, \omega_3) = -\frac{C_\Delta}{2}\left\{ -\ln\left[1 - \frac{\omega_1^2}{4\mu^2}\right] - \ln\left[1 - \frac{\omega_2^2}{4\mu^2}\right] + \ln\left[1 - \frac{\omega_3^2}{4\mu^2}\right]\right\}, \tag{B18}$$

$$\bar{\chi}_{xyxy}(\omega_1, \omega_2, \omega_3) = -\frac{C_\Delta}{2}\left\{ \ln\left[1 - \frac{\omega_1^2}{4\mu^2}\right] - \ln\left[1 - \frac{\omega_2^2}{4\mu^2}\right] - \ln\left[1 - \frac{\omega_3^2}{4\mu^2}\right]\right\}, \tag{B19}$$

$$\bar{\chi}_{xyyx}(\omega_1, \omega_2, \omega_3) = -\frac{C_\Delta}{2}\left\{ -\ln\left[1 - \frac{\omega_1^2}{4\mu^2}\right] + \ln\left[1 - \frac{\omega_2^2}{4\mu^2}\right] - \ln\left[1 - \frac{\omega_3^2}{4\mu^2}\right]\right\}. \tag{B20}$$

where

$$C_\Delta = \frac{N_f m \Delta^{(1)} \mathcal{M}^{(1)}}{24\pi\hbar^2}. \tag{B21}$$

Since $\Delta^{(1)}\mathcal{M}^{(1)} = [\Theta^{(1)}]^2$, we have $C_\Delta = C_\Theta$.

[1] K. Ishioka, M. Hase, M. Kitajima, L. Wirtz, A. Rubio, and H. Petek, Ultrafast electron-phonon decoupling in graphite, Phys. Rev. B **77**, 121402(R) (2008).

[2] Y. Murakami, P. Werner, N. Tsuji, and H. Aoki, Interaction quench in the holstein model: Thermalization crossover from electron- to phonon-dominated relaxation, Phys. Rev. B **91**, 045128 (2015).

[3] P. C. Hohenberg and B. I. Halperin, Theory of dynamic critical phenomena, Rev. Mod. Phys. **49**, 435 (1977).

[4] P. E. Dolgirev, M. H. Michael, A. Zong, N. Gedik, and E. Demler, Self-similar dynamics of order parameter fluctuations in pump-probe experiments, Phys. Rev. B **101**, 174306 (2020).

[5] Z. Sun and A. J. Millis, Transient Trapping into Metastable States in Systems with Competing Orders, Phys. Rev. X **10**, 021028 (2020).

[6] T. Huber, S. O. Mariager, A. Ferrer, H. Schäfer, J. A. Johnson, S. Grübel, A. Lübcke, L. Huber, T. Kubacka, C. Dornes, C. Laulhe, S. Ravy, G. Ingold, P. Beaud, J. Demsar, and S. L. Johnson, Coherent Structural Dynamics of a Prototypical Charge-Density-Wave-to-Metal Transition, Phys. Rev. Lett. **113**, 026401 (2014).

[7] F. Giorgianni, T. Cea, C. Vicario, C. P. Hauri, W. K. Withanage, X. Xi, and L. Benfatto, Leggett mode controlled by light pulses, Nat. Phys. **15**, 341 (2019).

[8] A. de la Torre, D. M. Kennes, M. Claassen, S. Gerber, J. W. McIver, and M. A. Sentef, Colloquium: Nonthermal pathways to ultrafast control in quantum materials, Rev. Mod. Phys. **93**, 041002 (2021).

[9] C. Vaswani, L.-L. Wang, D. H. Mudiyanselage, Q. Li, P. M. Lozano, G. D. Gu, D. Cheng, B. Song, L. Luo, R. H. J. Kim, C. Huang, Z. Liu, M. Mootz, I. E. Perakis, Y. Yao, K. M. Ho, and J. Wang, Light-Driven Raman Coherence as a Nonthermal Route to Ultrafast Topology Switching in a Dirac Semimetal, Phys. Rev. X **10**, 021013 (2020).

[10] T. Oka and H. Aoki, Photovoltaic hall effect in graphene, Phys. Rev. B **79**, 081406(R) (2009).

[11] A. P. Itin and M. I. Katsnelson, Effective Hamiltonians for Rapidly Driven Many-Body Lattice Systems: Induced Exchange Interactions and Density-Dependent Hoppings, Phys. Rev. Lett. **115**, 075301 (2015).

[12] H. Aoki, N. Tsuji, M. Eckstein, M. Kollar, T. Oka, and P. Werner, Nonequilibrium dynamical mean-field theory and its applications, Rev. Mod. Phys. **86**, 779 (2014).

[13] M. Lejman, G. Vaudel, I. C. Infante, P. Gemeiner, V. E. Gusev, B. Dkhil, and P. Ruello, Giant ultrafast photo-induced shear strain in ferroelectric BiFeO₃, Nat. Commun. **5**, 4301 (2014).

[14] T. F. Nova, A. S. Disa, M. Fechner, and A. Cavalleri, Metastable ferroelectricity in optically strained SrTiO₃, Science **364**, 1075 (2019).

[15] J. G. Horstmann, H. Böckmann, B. Wit, F. Kurtz, G. Storeck, and C. Ropers, Coherent control of a surface structural phase transition, Nature (London) **583**, 232 (2020).

[16] A. S. Disa, T. F. Nova, and A. Cavalleri, Engineering crystal structures with light, Nat. Phys. **17**, 1087 (2021).

[17] M. Henstridge, M. Först, E. Rowe, M. Fechner, and A. Cavalleri, Nonlocal nonlinear phononics, Nat. Phys. **18**, 457 (2022).

[18] P. H. Tan, W. P. Han, W. J. Zhao, Z. H. Wu, K. Chang, H. Wang, Y. F. Wang, N. Bonini, N. Marzari, N. Pugno, G. Savini, A. Lombardo, and A. C. Ferrari, The shear mode of multilayer graphene, Nat. Mater. **11**, 294 (2012).

[19] A. C. Ferrari and D. M. Basko, Raman spectroscopy as a versatile tool for studying the properties of graphene, Nat. Nanotechnol. **8**, 235 (2013).

[20] X. Zhang, W. P. Han, J. B. Wu, S. Milana, Y. Lu, Q. Q. Li, A. C. Ferrari, and P. H. Tan, Raman spectroscopy of shear and layer breathing modes in multilayer MoS₂, Phys. Rev. B **87**, 115413 (2013).

[21] H. Zeng, B. Zhu, K. Liu, J. Fan, X. Cui, and Q. M. Zhang, Low-frequency raman modes and electronic excitations in atomically thin MoS₂ films, Phys. Rev. B **86**, 241301(R) (2012).

[22] K. H. Michel and B. Verberck, Theory of the evolution of phonon spectra and elastic constants from graphene to graphite, Phys. Rev. B **78**, 085424 (2008).

[23] K. H. Michel and B. Verberck, Theory of rigid-plane phonon modes in layered crystals, Phys. Rev. B **85**, 094303 (2012).

[24] Y. Zhao, X. Luo, H. Li, J. Zhang, P. T. Araujo, C. K. Gan, J. Wu, H. Zhang, S. Y. Quek, M. S. Dresselhaus, and Q. Xiong, Interlayer breathing and shear modes in few-trilayer MoS₂ and WSe₂, Nano Lett. **13**, 1007 (2013).

[25] G. Wang, X. Li, Y. Wang, Z. Zheng, Z. Dai, X. Qi, L. Liu, Z. Cheng, Z. Xu, P. Tan, and Z. Zhang, Interlayer coupling behaviors of boron doped multilayer graphene, J. Phys. Chem. C **121**, 26034 (2017).

[26] G. Pizzi, S. Milana, A. C. Ferrari, N. Marzari, and M. Gibertini, Shear and breathing modes of layered materials, ACS Nano **15**, 12509 (2021).

[27] M. Y. Zhang, Z. X. Wang, Y. N. Li, L. Y. Shi, D. Wu, T. Lin, S. J. Zhang, Y. Q. Liu, Q. M. Liu, J. Wang, T. Dong, and N. L. Wang, Light-induced subpicosecond lattice symmetry switch in MoTe$_2$, Phys. Rev. X **9**, 021036 (2019).

[28] S. Ji, O. Grånäs, and J. Weissenrieder, Manipulation of stacking order in Td-WTe$_2$ by ultrafast optical excitation, ACS Nano **15**, 8826 (2021).

[29] E. J. Sie, C. M. Nyby, C. D. Pemmaraju, S. J. Park, X. Shen, J. Yang, M. C. Hoffmann, B. K. Ofori-Okai, R. Li, A. H. Reid, S. Weathersby, E. Mannebach, N. Finney, D. Rhodes, D. Chenet, A. Antony, L. Balicas, J. Hone, T. P. Devereaux, T. F. Heinz *et al.*, An ultrafast symmetry switch in a Weyl semimetal, Nature (London) **565**, 61 (2019).

[30] M. Born, K. Huang, and M. Lax, Dynamical theory of crystal lattices, Am. J. Phys. **23**, 474 (1955).

[31] G. Lanzani, G. Cerullo, and S. De Silvestri, *Coherent Vibrational Dynamics* (CRC Press, Boca Raton, 2007).

[32] T. Dekorsy, G. C. Cho, and H. Kurz, Coherent phonons in condensed media, in *Light Scattering in Solids VIII: Fullerenes, Semiconductor Surfaces, Coherent Phonons*, edited by M. Cardona and G. Güntherodt (Springer, Berlin, 2000), pp. 169–209.

[33] M. Hase, M. Kitajima, A. M. Constantinescu, and H. Petek, The birth of a quasiparticle in silicon observed in time–frequency space, Nature (London) **426**, 51 (2003).

[34] K. Ishioka, M. Hase, M. Kitajima, and H. Petek, Coherent optical phonons in diamond, Appl. Phys. Lett. **89**, 231916 (2006).

[35] H. J. Zeiger, J. Vidal, T. K. Cheng, E. P. Ippen, G. Dresselhaus, and M. S. Dresselhaus, Theory for displacive excitation of coherent phonons, Phys. Rev. B **45**, 768 (1992).

[36] T. Pfeifer, T. Dekorsy, W. Kütt, and H. Kurz, Generation mechanism for coherent lo phonons in surface-space-charge fields of iii-v-compounds, Appl. Phys. A **55**, 482 (1992).

[37] A. V. Kuznetsov and C. J. Stanton, Theory of Coherent Phonon Oscillations in Semiconductors, Phys. Rev. Lett. **73**, 3243 (1994).

[38] A. V. Kuznetsov and C. J. Stanton, Coherent phonon oscillations in gaas, Phys. Rev. B **51**, 7555 (1995).

[39] T. E. Stevens, J. Kuhl, and R. Merlin, Coherent phonon generation and the two stimulated raman tensors, Phys. Rev. B **65**, 144304 (2002).

[40] G. A. Garrett, T. F. Albrecht, J. F. Whitaker, and R. Merlin, Coherent THz Phonons Driven by Light Pulses and the Sb Problem: What is the Mechanism? Phys. Rev. Lett. **77**, 3661 (1996).

[41] R. Merlin, Generating coherent thz phonons with light pulses, Solid State Commun. **102**, 207 (1997).

[42] J. Zhang, J. Han, G. Peng, X. Yang, X. Yuan, Y. Li, J. Chen, W. Xu, K. Liu, Z. Zhu, W. Cao, Z. Han, J. Dai, M. Zhu, S. Qin, and K. S. Novoselov, Light-induced irreversible structural phase transition in trilayer graphene, Light Sci. Appl. **9**, 174 (2020).

[43] D. Soranzio, M. Peressi, R. J. Cava, F. Parmigiani, and F. Cilento, Ultrafast broadband optical spectroscopy for quantifying subpicometric coherent atomic displacements in WTe$_2$, Phys. Rev. Res. **1**, 032033(R) (2019).

[44] T. Fukuda, K. Makino, Y. Saito, P. Fons, A. V. Kolobov, K. Ueno, and M. Hase, Ultrafast dynamics of the low frequency shear phonon in 1T′-MoTe$_2$, Appl. Phys. Lett. **116**, 093103 (2020).

[45] P. Hein, S. Jauernik, H. Erk, L. Yang, Y. Qi, Y. Sun, C. Felser, and M. Bauer, Mode-resolved reciprocal space mapping of electron-phonon interaction in the Weyl semimetal candidate Td-WTe$_2$, Nat. Commun. **11**, 2613 (2020).

[46] H. Rostami, Theory for shear displacement by light-induced raman force in bilayer graphene, Phys. Rev. B **106**, 155405 (2022).

[47] M. S. Dresselhaus, G. Dresselhaus, and A. Jorio, *Group theory: Application to the Physics of Condensed Matter* (Springer Science & Business Media, Berlin, 2007).

[48] G. D. Mahan, *Many-Particle Physics* (Springer US, New York, 1995).

[49] T. P. Devereaux and R. Hackl, Inelastic light scattering from correlated electrons, Rev. Mod. Phys. **79**, 175 (2007).

[50] E. McCann and V. I. Fal'ko, Landau-Level Degeneracy and Quantum Hall Effect in a Graphite Bilayer, Phys. Rev. Lett. **96**, 086805 (2006).

[51] H. Rostami and R. Asgari, Electronic structure and layer-resolved transmission of bilayer graphene nanoribbon in the presence of vertical fields, Phys. Rev. B **88**, 035404 (2013).

[52] E. McCann and M. Koshino, The electronic properties of bilayer graphene, Rep. Prog. Phys. **76**, 056503 (2013).

[53] K. Ishikawa and T. Ando, Optical phonon interacting with electrons in carbon nanotubes, J. Phys. Soc. Jpn. **75**, 084713 (2006).

[54] E. Cappelluti and G. Profeta, Hopping-resolved electron-phonon coupling in bilayer graphene, Phys. Rev. B **85**, 205436 (2012).

[55] D. M. Basko, Calculation of the RamanGpeak intensity in monolayer graphene: role of ward identities, New J. Phys. **11**, 095011 (2009).

[56] G. Giuliani and G. Vignale, *Quantum Theory of the Electron Liquid* (Cambridge University Press, Cambridge, 2005).

[57] C. H. Lui, K. F. Mak, J. Shan, and T. F. Heinz, Ultrafast Photoluminescence from Graphene, Phys. Rev. Lett. **105**, 127404 (2010).

[58] A. Tomadin, D. Brida, G. Cerullo, A. C. Ferrari, and M. Polini, Nonequilibrium dynamics of photoexcited electrons in graphene: Collinear scattering, auger processes, and the impact of screening, Phys. Rev. B **88**, 035430 (2013).

[59] D. Brida, A. Tomadin, C. Manzoni, Y. J. Kim, A. Lombardo, S. Milana, R. R. Nair, K. S. Novoselov, A. C. Ferrari, G. Cerullo, and M. Polini, Ultrafast collinear scattering and carrier multiplication in graphene, Nat. Commun. **4**, 1987 (2013).

[60] A. Tomadin, S. M. Hornett, H. I. Wang, E. M. Alexeev, A. Candini, C. Coletti, D. Turchinovich, M. Kläui, M. Bonn, F. H. L. Koppens, E. Hendry, M. Polini, and K.-J. Tielrooij, The ultrafast dynamics and conductivity of photoexcited graphene at different fermi energies, Sci. Adv. **4**, eaar5313 (2018).

[61] F. Andreatta, H. Rostami, A. G. Cabo, M. Bianchi, C. E. Sanders, D. Biswas, C. Cacho, A. J. H. Jones, R. T. Chapman, E. Springate, P. D. C. King, J. A. Miwa, A. Balatsky, S. Ulstrup, and P. Hofmann, Transient hot electron dynamics in single-layer tas$_2$, Phys. Rev. B **99**, 165421 (2019).

[62] F. Giustino, Electron-phonon interactions from first principles, Rev. Mod. Phys. **89**, 015003 (2017).

[63] S. Ulstrup, J. C. Johannsen, F. Cilento, J. A. Miwa, A. Crepaldi, M. Zacchigna, C. Cacho, R. Chapman, E. Springate, S. Mammadov, F. Fromm, C. Raidel, T. Seyller, F. Parmigiani,

M. Grioni, P. D. C. King, and P. Hofmann, Ultrafast Dynamics of Massive Dirac Fermions in Bilayer Graphene, Phys. Rev. Lett. **112**, 257401 (2014).

[64] L. Luo, D. Cheng, B. Song, L.-L. Wang, C. Vaswani, P. M. Lozano, G. Gu, C. Huang, R. H. J. Kim, Z. Liu, J.-M. Park, Y. Yao, K. Ho, I. E. Perakis, Q. Li, and J. Wang, A light-induced phononic symmetry switch and giant dissipationless topological photocurrent in $ZrTe_5$, Nat. Mater. **20**, 329 (2021).

[65] F. Giorgianni, M. Udina, T. Cea, E. Paris, M. Caputo, M. Radovic, L. Boie, J. Sakai, C. W. Schneider, and S. L. Johnson, Terahertz displacive excitation of a coherent raman-active phonon in V_2O_3, Commun. Phys. **5**, 103 (2022).

[66] Z. Zheng, Q. Ma, Z. Bi, S. de la Barrera, M.-H. Liu, N. Mao, Y. Zhang, N. Kiper, K. Watanabe, T. Taniguchi, J. Kong, W. A. Tisdale, R. Ashoori, N. Gedik, L. Fu, S.-Y. Xu, and P. Jarillo-Herrero, Unconventional ferroelectricity in moiréheterostructures, Nature (London) **588**, 71 (2020).

[67] C. R. Woods, P. Ares, H. Nevison-Andrews, M. J. Holwill, R. Fabregas, F. Guinea, A. K. Geim, K. S. Novoselov, N. R. Walet, and L. Fumagalli, Charge-polarized interfacial superlattices in marginally twisted hexagonal boron nitride, Nat. Commun. **12**, 347 (2021).

[68] K. Yasuda, X. Wang, K. Watanabe, T. Taniguchi, and P. Jarillo-Herrero, Stacking-engineered ferroelectricity in bilayer boron nitride, Science **372**, 1458 (2021).

[69] M. Vizner Stern, Y. Waschitz, W. Cao, I. Nevo, K. Watanabe, T. Taniguchi, E. Sela, M. Urbakh, O. Hod, and M. Ben Shalom, Interfacial ferroelectricity by van der waals sliding, Science **372**, 1462 (2021).

[70] Z. Fei, W. Zhao, T. A. Palomaki, B. Sun, M. K. Miller, Z. Zhao, J. Yan, X. Xu, and D. H. Cobden, Ferroelectric switching of a two-dimensional metal, Nature (London) **560**, 336 (2018).

[71] P. Sharma, F.-X. Xiang, D.-F. Shao, D. Zhang, E. Y. Tsymbal, A. R. Hamilton, and J. Seidel, A room-temperature ferroelectric semimetal, Sci. Adv. **5**, eaax5080 (2019).

[72] W. X. Zhou and A. Ariando, Review on ferroelectric/polar metals, Jpn. J. Appl. Phys. **59**, SI0802 (2020).

[73] W. Qin and A. H. MacDonald, In-Plane Critical Magnetic Fields in Magic-Angle Twisted Trilayer Graphene, Phys. Rev. Lett. **127**, 097001 (2021).

[74] J. Liang, D. Yang, J. Wu, J. I. Dadap, K. Watanabe, T. Taniguchi, and Z. Ye, Optically Probing the Asymmetric Interlayer Coupling in Rhombohedral-Stacked MoS_2 Bilayer, Phys. Rev. X **12**, 041005 (2022).

[75] H. Rostami, M. I. Katsnelson, G. Vignale, and M. Polini, Gauge invariance and ward identities in nonlinear response theory, Ann. Phys. (NY) **431**, 168523 (2021).